

JGR Solid Earth

RESEARCH ARTICLE

10.1029/2020JB020988

Key Points:

- Gem-bearing reaction zones in Mogok marbles record three episodes of fluid infiltration each separated in time by 7–13 Ma
- Initial fluid infiltration drives dolomite-consuming reactions and produces high-permeability zones that channelize later fluid transport
- Effect of multiple fluid infiltration episodes on metamorphic CO₂ release from marbles in orogenic belts is assessed

Supporting Information:

- Supporting Information S1

Correspondence to:

S. Guo,
guoshun@mail.iggcas.ac.cn

Citation:

Guo, S., Chu, X., Hermann, J., Chen, Y., Li, Q., Wu, F., et al. (2021). Multiple episodes of fluid infiltration along a single metasomatic channel in metacarbonates (Mogok metamorphic belt, Myanmar) and implications for CO₂ release in orogenic belts. *Journal of Geophysical Research: Solid Earth*, 126, e2020JB020988. <https://doi.org/10.1029/2020JB020988>

Received 18 SEP 2020

Accepted 20 NOV 2020

Multiple Episodes of Fluid Infiltration Along a Single Metasomatic Channel in Metacarbonates (Mogok Metamorphic Belt, Myanmar) and Implications for CO₂ Release in Orogenic Belts

Shun Guo^{1,2} , Xu Chu³, Joerg Hermann⁴ , Yi Chen^{1,2} , Qiuli Li¹ , Fuyuan Wu¹, Chuanzhou Liu^{1,2}, and Kyaing Sein⁵

¹State Key Laboratory of Lithospheric Evolution, Institute of Geology and Geophysics, Chinese Academy of Sciences, Beijing, China, ²CAS Center for Excellence in Tibetan Plateau Earth Sciences, Beijing, China, ³Department of Earth Sciences, University of Toronto, Toronto, ON, Canada, ⁴Institute of Geological Sciences, University of Bern, Bern, Switzerland, ⁵Myanmar Geosciences Society, Hlaing University Campus, Yangon, Myanmar

Abstract Fluid infiltration into metacarbonates is a key mechanism to induce orogenic decarbonation, which influences the global carbon cycle and long-term climate evolution. Little is known regarding the fluid pathways during episodic infiltration events and how flow patterns control time-integrated CO₂ outflux. We investigate the “vein-like” polycrystalline mineral reaction zones (PMRZs) in dolomite marbles (Mogok metamorphic belt, Myanmar), which are formed by metasomatism via the infiltration of Si–Al–K–Ti–Zr-bearing fluids. The petrographic textures and mineral U–Pb chronology reveal three episodes of fluid influx in a single PMRZ: (1) the initial episode (Stage-I) transformed most dolomite into Mg-rich silicates/oxides and calcite at ~35–36 Ma indicated by baddeleyite cores; (2) baddeleyite rims gave ages of ~23–24 Ma, representing a subsequent infiltration episode (Stage-II) that modified Stage-I minerals via a dissolution–precipitation mechanism; (3) the final episode (Stage-III) is recorded by zircon replacing baddeleyite, which yielded ages of ~17 Ma. Stage-III fluid has a higher SiO₂ activity and X_{CO_2} [CO₂/(CO₂ + H₂O)] than Stage-I/Stage-II fluids. Thermodynamic and mass-balance analyses indicate that Stage-I infiltration causes >62–67% loss of CO₂ by both dolomite-consuming reactions and calcite dissolution, whereas the latter two infiltration episodes induce <12–18% loss of CO₂ via calcite dissolution. Our results provide compelling evidence that repeated episodes of infiltration (each separated in time by 7–13 Ma) occurred along a single channel in marbles. The initial infiltration episode may create high-permeability regions, offering favorable channels for later-stage fluids that transfer obviously less CO₂ than the initial metasomatism. This considerably complicates a quantitative assessment of CO₂ liberation from metacarbonates during orogenesis.

1. Introduction

Metamorphic release of CO₂ from collisional orogens plays a fundamental role in global carbon cycling, and thus might exert a significant influence on climate variations over geological times (e.g., Bickle, 1996; Evans, 2011; Ferry, 2016; Groppo et al., 2017; Kerrick & Caldeira, 1998; Skelton, 2013; Stewart et al., 2019; Svensen & Jamtveit, 2010). Recent field-based investigations and quantitative modeling reveal that the magnitude of orogenic CO₂ outflux is comparable with, or even higher than, the CO₂ losses from mid-ocean ridge and island arcs (e.g., Becker et al., 2008; Skelton, 2011; Stewart & Ague, 2018). While the orogenic CO₂ liberation can be achieved by regional metamorphism of carbonate-rich rocks in closed systems (e.g., Groppo et al., 2013, 2017), many studies indicate that significant decarbonation is related to the infiltration of external metamorphic–magmatic fluids into metacarbonate rocks (e.g., Ague, 2014; Carter & Dasgupta, 2018; Evans, 2011; Ferry, 2016; Ganino & Arndt, 2009; Kerrick, 1977; Stewart et al., 2019). The influx of aqueous fluids lowers the activity of CO₂ and introduces silica and other components into a carbonate lithology, whereby silicate minerals crystallize and CO₂ is released by carbonate-consuming reactions (e.g., Bégué et al., 2020; Ferry, 2016) or carbonate dissolution (e.g., Ague & Nicolescu, 2014; Chu et al., 2019). Thus, understanding the fluid flow regime, metasomatic reaction progress, as well as time-resolved evolution is crucial for constraining the CO₂ outflux during orogenesis (e.g., Ague, 2014; Baumgartner & Ferry, 1991; Evans, 2011; Ferry et al., 2013; Skelton, 2011).

It is widely recognized that the infiltration of metamorphic–magmatic fluids in collisional orogenic belts is typically episodic and likely to occur at distinct evolution stages and pressure–temperature (P–T) conditions throughout the entire orogenic cycle (Ague, 2014). In this context, orogenic metacarbonate rocks may experience multiple-stage decarbonation events and the total amount of released CO₂ from these rocks may reflect a cumulative result of decarbonation by multiple pulses of chemically distinct fluids. However, how the episodic fluids flow in metacarbonate rocks (e.g., along single vs. disparate channels) and how the fluid flow patterns influence CO₂ release during orogenic metamorphism are largely unknown.

In general, the infiltration of H₂O-rich fluids into metacarbonate lithologies gives rise to the metasomatic formation of reaction zones or selvages, some of which are important resources of (skarn-type) ore deposits and gemstones (e.g., Jamtveit et al., 1993; Kerrick, 1977; Themelis, 2008). These reaction zones or selvages provide an excellent opportunity to understand the fluid flow pathways and CO₂-producing reactions. Especially, the compositional zoning and replacement textures of minerals in the reaction zones may record discrete episodes of fluid flow (e.g., Bégue et al., 2019, 2020; Putnis, 2009; Putnis & Austrheim, 2010). Precise dating of fluid–rock interactions is the premise to uncover multiple fluid pulses and the interplay between the fluid flow and CO₂ outflux (Ague, 2014). However, due to a lack of suitable mineral chronometers, fluid infiltration events in carbonate rocks are notoriously difficult to date (e.g., Cliff et al., 1993; Williams et al., 1996; Wu et al., 2006). Therefore, clarifying the time-resolved fluid flow history in such metasomatized rocks is extremely challenging (Villa & Williams, 2013).

In this study, we focus on representative reaction zones formed by metasomatism via the infiltration of channelized fluids into dolomite marbles from the Mogok metamorphic belt (MMB), Myanmar. We present comprehensive investigations of the petrology, geochemistry, and baddeleyite/zircon chronology of the metasomatized rocks that are linked to thermodynamic modeling in order to reconstruct the fluid infiltration history and quantify the CO₂ release from metacarbonate rocks during multiple fluid influxes. Three episodes of fluid infiltration along a single flow pathway, each separated in time by ~7–13 Ma, are recognized in the marbles. We propose that the first-stage fluid infiltration dominates the geometry of reaction zones and CO₂ outflux during multiple metasomatism of orogenic marbles.

2. Geological Setting

The MMB (Figure 1a) is located in central Myanmar and extends for ~1500 km from the Andaman Sea north to the eastern Himalayan syntaxis (e.g., Barley et al., 2003; Gardiner et al., 2018; Mitchell et al., 2007; Searle et al., 2007). The MMB has long been of interest for geologists because this belt produces a variety of the world's finest colored gemstones, e.g., ruby, sapphire, and spinel (Themelis, 2008). This elongated (~50-km wide) and sigmoidal belt is distributed along the northwestern margin of the Shan Plateau and southwards between the Shan Scarp and Sagaing fault. The MMB mainly comprises a sequence of high-grade (amphibolite-to granulite-facies) metasedimentary and metaigneous rocks (Mitchell et al., 2012, 2007; Searle et al., 2017). The formation and evolution of the MMB are associated with the closure of the Neo-Tethys ocean, India–Asia collision, and post-collision extension and uplift (Searle et al., 2017).

The main lithologies of the MMB include ortho-gneisses and para-gneisses, migmatites, schists, marbles, and calc-silicate rocks (Mitchell et al., 2007; Searle et al., 2017). The peak metamorphic P–T conditions are ~5 kbar and 625–680°C for the gneisses in the Kyanigan area (Searle et al., 2007), 6–10 kbar and 780–850°C for the gneisses in the Sagaing town (Win et al., 2016), and ~8 kbar and >780–810°C for the marbles in the Thabeikgyin area (Thu & Enami, 2018). Previous age determinations indicate that the MMB metamorphism occurred during the Tertiary, with ages ranging from 60 to 31 Ma (Searle et al., 2017). Intrusions of granitoid bodies as well as leucosomes, dykes, hydrothermal veins, and pegmatites can be found in all the units of the MMB (e.g., Mitchell et al., 2012; Searle et al., 2017, 2020). In contact zones between the marbles and intrusions, metasomatic skarns develop by the infiltration of fluids/melts. The metasomatism may form various mineralogical reaction zones where rare gems are produced (Guo et al., 2016; Searle et al., 2020; Themelis, 2008).

The study area is located in Nayaung Oke-Sedawgyi (Figure 1a), ~20 km north of Mandalay. The Nayaung Oke-Sedawgyi area is mainly composed of (impure) marbles, calc-silicate rocks, gneisses, and schists, with small amounts of low-grade metamorphic rocks, sedimentary rocks, and intrusions (Figure 1b). Zircon

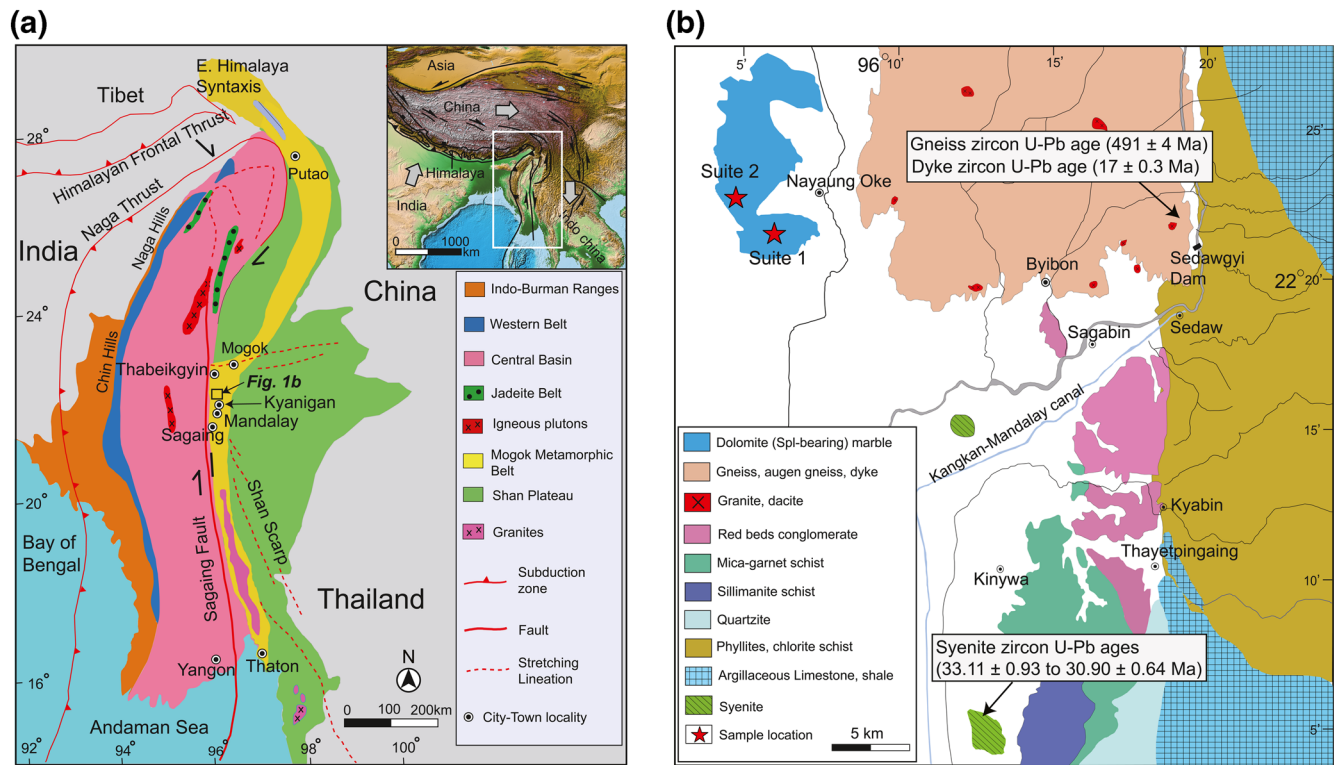


Figure 1. (a) A schematic geological map (modified from Themelis (2008)) showing main terrane boundaries of Myanmar and the distribution of the Mogok metamorphic belt (MMB). (b) A simplified geological map (modified from Mitchell et al. (2012)) of the Nayaung Oke-Sedawgyi area showing the lithologic distribution and sample localities. Age data of gneiss and dyke are from Mitchell et al. (2012) and age data of syenite are from Barley et al. (2003).

U–Pb dating of the Sedawgyi gneisses gave a Cambrian protolith age of 491 ± 4 Ma (Figure 1b; Mitchell et al., 2012). Analyses on a biotite granite dyke that might form by the anatexis of gneisses yielded a zircon U–Pb age of 17.0 ± 0.3 Ma (Mitchell et al., 2012). Barley et al. (2003) reported syntectonic deformed hornblende syenites with emplacement ages of 33.11 ± 0.93 to 30.90 ± 0.64 Ma (Figure 1b). Pure white-colored dolomite marbles are widely distributed in the Nayaung Oke area and are speculated to be the early-Jurassic metamorphic products of mid-Permian to Triassic deposited carbonates (Mitchell et al., 2012). The contact relationship between the marbles and gneisses in the field is not clear due to vegetation. Abundant dark-colored, vein-like, polycrystalline mineral reaction zones (PMRZs) are observed in marbles (Figures 2a and 2b). The PMRZs generally occur as isolated, irregularly shaped bands in marbles, which are typically on the order of 3–40 cm in width and 0.5–10 m in length. The interface between the PMRZs and marbles is typically sharp and the mineralogical front usually exhibits an undulated morphology (Figures 2c and 2d). Most of PMRZs contain high abundances of gem-level (pink-purple) crystals of spinel (up to 2 cm in size), forsterite, and phlogopite (Figures 2d–2f). The PMRZs formed by metasomatism when the reactive fluids infiltrated the marbles along the high-permeability fractures, and these reaction zones represent the flow pathways of infiltrating fluids. Moreover, preexisting compositional layers or fracture-filling materials (directly precipitated from a fluid in central fractures, e.g., Bucher-Nurminen, 1989) are not found in the PMRZs (Figure 2c), indicating that the PMRZs only represent the replaced portions (selvages) of the dolomite marbles.

3. Sample Description and Petrology

The investigated samples were collected from a marble quarry. Two suites of samples from different marble blocks were collected (Figures 2a and 2b). Each suite contains two samples of marble (13MDL73 and 13MDL74 for Suite 1; 16MDL6 and 16MDL7 for Suite 2) and three samples of PMRZ (13MDL76-A, 13MDL76-B, and 13MDL76-C for Suite 1; 16MDL5-A, 16MDL5-B, and 16MDL5-C for Suite 2). Mineral

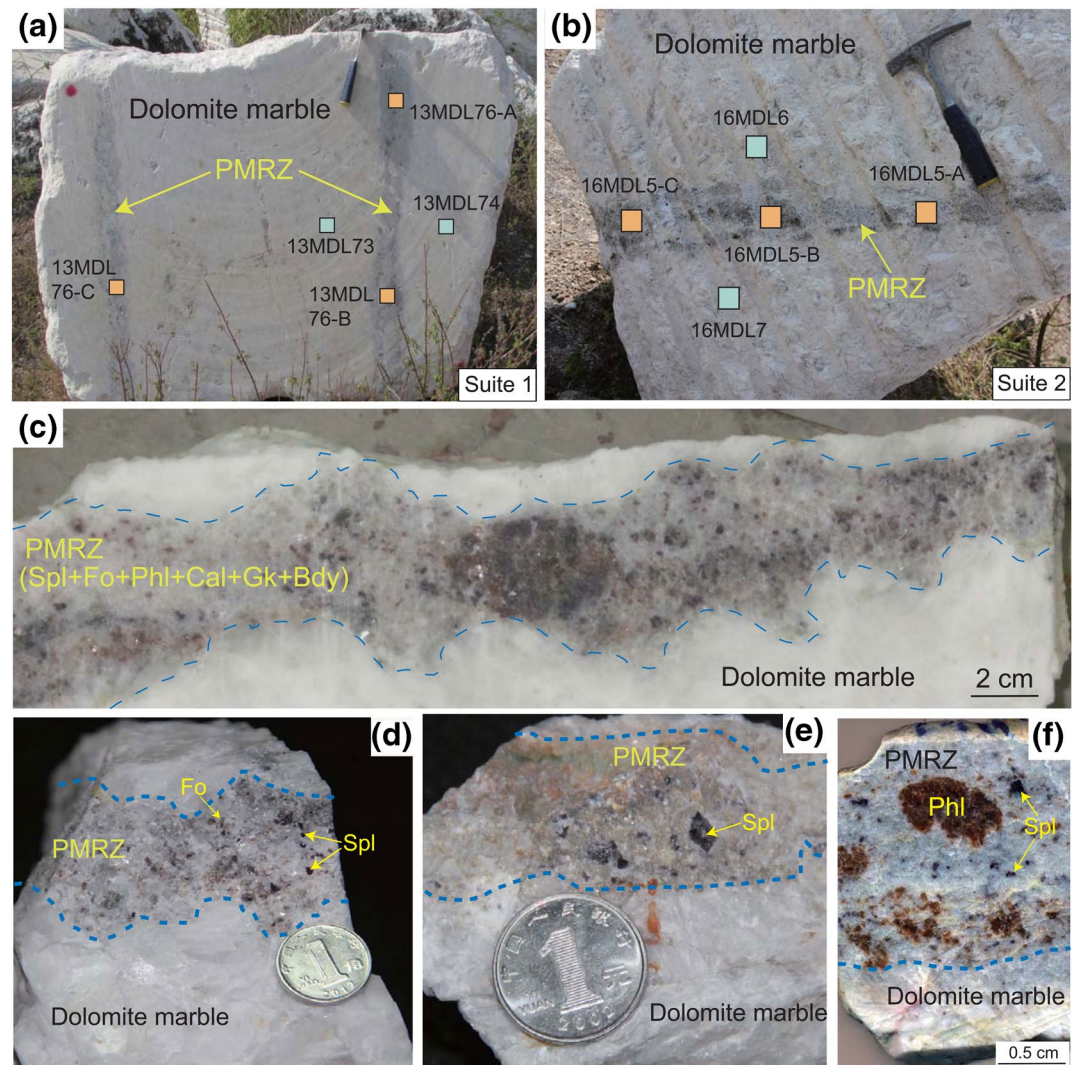


Figure 2. Field outcrops (a) and (b) and hand specimens (c)–(f) of polycrystalline mineral reaction zone (PMRZ) in dolomite marbles. (a) and (b) Distribution of dark-colored, PMRZs in white-colored marbles. Two suites of samples were collected and detailed sampling locations and sample sizes were labeled. (c) Sharp boundaries between the PMRZ and marbles and the undulated morphology of mineralogical front in a polished hand specimen. Note that no preexisting compositional layers or fracture-filling materials (directly precipitated from a fluid) are found in the PMRZ. (d) Spinel and forsterite in the PMRZ hosted by coarse-grained dolomite marbles. (e) Spinel porphyroblasts and (f) phlogopite aggregates in the PMRZs.

assemblages and abundances of the samples are presented in Table S1. Mineral abbreviations are after Whitney and Evans (2010).

The host marbles are dominantly composed of coarse-grained dolomite (up to 4 cm in size). In addition, only rare forsterite is found (<1 vol.%). Porphyroblasts of dolomite typically show an anhedral shape with rhombohedral cleavage (Figures 3a and 3b). No accessory minerals (e.g., zircon, baddeleyite, rutile, and apatite) are found in the host marbles.

The PMRZ samples are mainly composed of spinel, forsterite, phlogopite, calcite, accessory geikielite, baddeleyite, rutile, and zircon. Spinel (7–18 vol.%) occurs as coarse-grained porphyroblasts or fine-grained matrix minerals and contains inclusions of phlogopite, calcite, and forsterite (Figure 3c). Forsterite (18–36 vol.%) is in textural equilibrium with spinel and calcite and occurs as rounded to subrounded porphyroblasts or matrix minerals (Figures 3d and 3e). Forsterite contains inclusions of calcite and spinel (Figure 3d) and no replacement of forsterite by serpentine is observed. Phlogopite (3–17 vol.%) exhibits a flaky shape and occurs

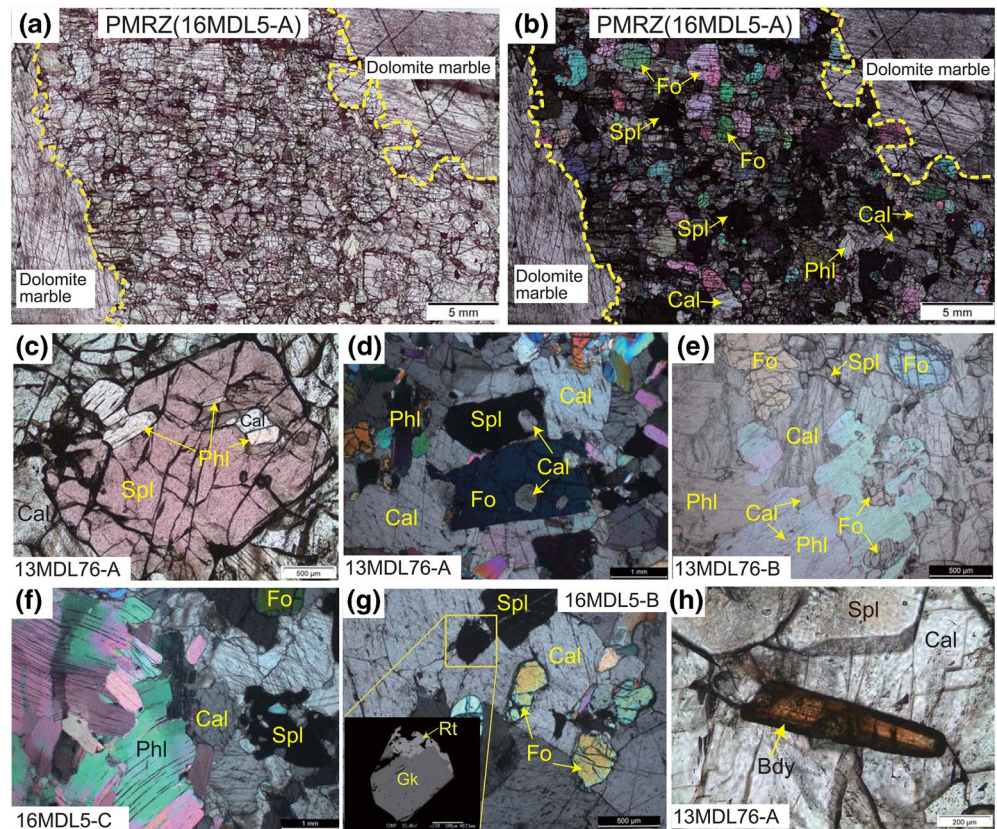


Figure 3. Photomicrographs and BSE image of PMRZs in the MMB marbles. (a) and (b) Photomicrographs of a thin section showing the PMRZ mineral assemblage of Fo + Spl + Phl + Cal. (c) A spinel porphyroblast containing inclusions of phlogopite and calcite. (d) Coexistence of spinel, forsterite, phlogopite, and calcite. Calcite inclusions are observed in both forsterite and spinel. (e) Forsterite and calcite inclusions in phlogopite porphyroblasts. (f) Polycrystalline aggregates of phlogopite in the PMRZ. (g) Geikielite occurs as an accessory mineral in the PMRZ. Insert BSE image showing the partial replacement of geikielite by rutile. (h) Euhedral baddeleyite occurs as an accessory mineral and is in textural equilibrium with spinel and calcite. a, c, e, and h in plane-polarized light; b, d, f, and g in cross-polarized light.

either as fine-grained inclusions in spinel or as porphyroblasts containing calcite and forsterite (Figure 3e). In sample 16MDL5-C, phlogopite forms polycrystalline aggregates (Figure 3f). Calcite (36–47 vol.%) occurs either as fine-grained inclusions in spinel and silicate minerals or as an anhedral matrix mineral (Figures 3c and 3d). Relic dolomite (<2 vol.%) is only found in the regions near the boundaries of PMRZs and marbles and has much smaller grain sizes than dolomite in host marbles. Geikielite occurs as an anhedral matrix phase and occasionally contains inclusions of forsterite and spinel. Some geikielite grains are partially replaced by rutile (Figure 3g). Baddeleyite typically occurs as euhedral to subhedral grains in the PMRZs and is in textural equilibrium with forsterite, spinel, phlogopite, and calcite (Figure 3h).

4. Analytical Methods

4.1. Whole-Rock Major and Trace Elements

Whole-rock analyses were conducted at the Institute of Geology and Geophysics, Chinese Academy of Sciences (IGGCAS). The rock samples (Figures 2a and 2b) were first ground to powders (~40 g for each sample). For major elements, ~0.5 g sample powders were mixed with 5 g Li₂B₄O₇ powders, and then were heated and fused to a glass disk and measured using an Axios-Minerals sequential X-ray fluorescence spectrometer. The precision and accuracy of data were better than 5%, estimated from the repeated analyses of reference materials GSR-2 and GSR-3 and the duplicated analyses of the samples.

Trace elements were analyzed by inductively coupled plasma mass spectrometry (ICP-MS) with a Finnigan Mat ELEMENT spectrometer. The digestion procedure of samples is the same as that described by Guo et al. (2019). The analyses on three rock reference materials, GSR-1, GSR-2, and GSR-3, indicate that the accuracy of the data was better than 5% for most trace elements and the precision was better than 5% (RSD).

4.2. Mineral Composition, Element X-ray Maps, and Mineral Textures

Major element compositions of minerals were measured using a JEOL JXA-8100 electron probe micro-analyzer (EPMA) at the IGGCAS. The analyses were operated in wavelength-dispersion mode (WDS) with an acceleration voltage of 15 kV, a beam current of 10 nA, and a beam diameter of 1 μm . Natural and synthetic oxides were used as standards and the precision was better than 1.5% (1σ).

X-ray maps of Cr, Al, and Fe of spinel were acquired by WDS analyses using a Cameca-SXFive EPMA at the IGGCAS. The crystals used for Cr, Al, and Fe analyses were LLIF, TAP, and LIF, respectively. The operating conditions were a 15 kV acceleration voltage, a 100 nA beam current, and a dwell time per point of 50 ms.

Textural features of carbonates were examined using a RELIOTRON cathodoluminescence (CL) microscopy at the IGGCAS, with voltages of 5–8 kV and currents of 300–400 μA .

Trace elements of minerals were analyzed using a laser ablation ICP-MS (LA-ICP-MS) at the State Key Laboratory of Continental Dynamics, Northwest University. The instrument includes a GeoLas 200M laser-ablation system equipped with a 193 nm ArF excimer laser and an Agilent 7500a ICP-MS. A detailed analytical procedure can be found in Gao et al. (2002). Analyses were carried out using a spot size of 60 μm with a repetition rate of 10 Hz. ^{43}Ca was used as the internal standard for calcite and dolomite, ^{24}Mg was used for spinel and forsterite, and ^{29}Si was used for phlogopite. The USGS NIST 610 glass standard was used for external calibration and three USGS glasses (NIST 612, GSE-1G, and BCR-2G) were used as monitoring standards. Trace element data were calculated using GLITTER 4.0 Online Interactive Data Reduction developed by GEMOC, Macquarie University. The accuracy for the contents of most trace elements was better than 8%.

4.3. Baddeleyite and Zircon U–Pb Dating

The separated baddeleyite and zircon grains from two samples of PMRZ (13MDL76-A and 16MDL5-A) were cast into 25 mm resin mounts together with the corresponding standards. CL images of both minerals were obtained using a LEO1450VP scanning electron microscope at the IGGCAS to reveal their grain sizes, morphology, structure, and suitable spot locations for the U–Th–Pb isotopic analyses.

The baddeleyite and zircon dating were performed using a CAMECA 1280 secondary ion mass spectrometry (SIMS) at the IGGCAS. The instrument description and analytical procedures can be found in Li et al. (2009). An innovated oxygen flooding technique was applied to suppress the crystal orientation effect and to improve the analytical precision (Li et al., 2010). For the baddeleyite dating, the ion beam spot was $\sim 20 \times 30 \mu\text{m}$ in diameter. The Phalaborwa baddeleyite reference (~ 2060 Ma, Heaman & LeCheminant, 1993) was measured between every three sample spot analyses to calibrate Pb/U ratios and U contents. For the zircon dating, analyses of zircon standards Plesovice and 91500 were interspersed with unknown grains. Each measurement consisted of seven cycles. Pb/U calibration was performed relative to the standard Plesovice (Sláma et al., 2008) and U and Th contents were calibrated against the standard 91500 (Wiedenbeck et al., 1995). The ion beam spot was $\sim 15 \times 20 \mu\text{m}$ in diameter (Liu et al., 2011). Tera-Wasserburg concordia diagrams and calculated weighted mean ages were produced using the program ISOPLOT/Ex 3.23 (Ludwig, 2003). The measurements of a zircon standard Qinghu yielded weighted average $^{206}\text{Pb}/^{238}\text{U}$ and $^{207}\text{Pb}/^{235}\text{U}$ ages of 160.5 ± 1.4 Ma (2σ) and 161.2 ± 1.6 Ma (2σ), respectively, which are in good agreement with its recommended ages within errors (Li et al., 2013).

5. Results

5.1. Whole-Rock Major and Trace Elements

The whole-rock compositions of four marble samples and six PMRZ samples are presented in Table S2. The marbles are mainly composed of CaO (30–31 wt%), MgO (20–21 wt%), and CO₂ (47–48 wt%) and exhibit a

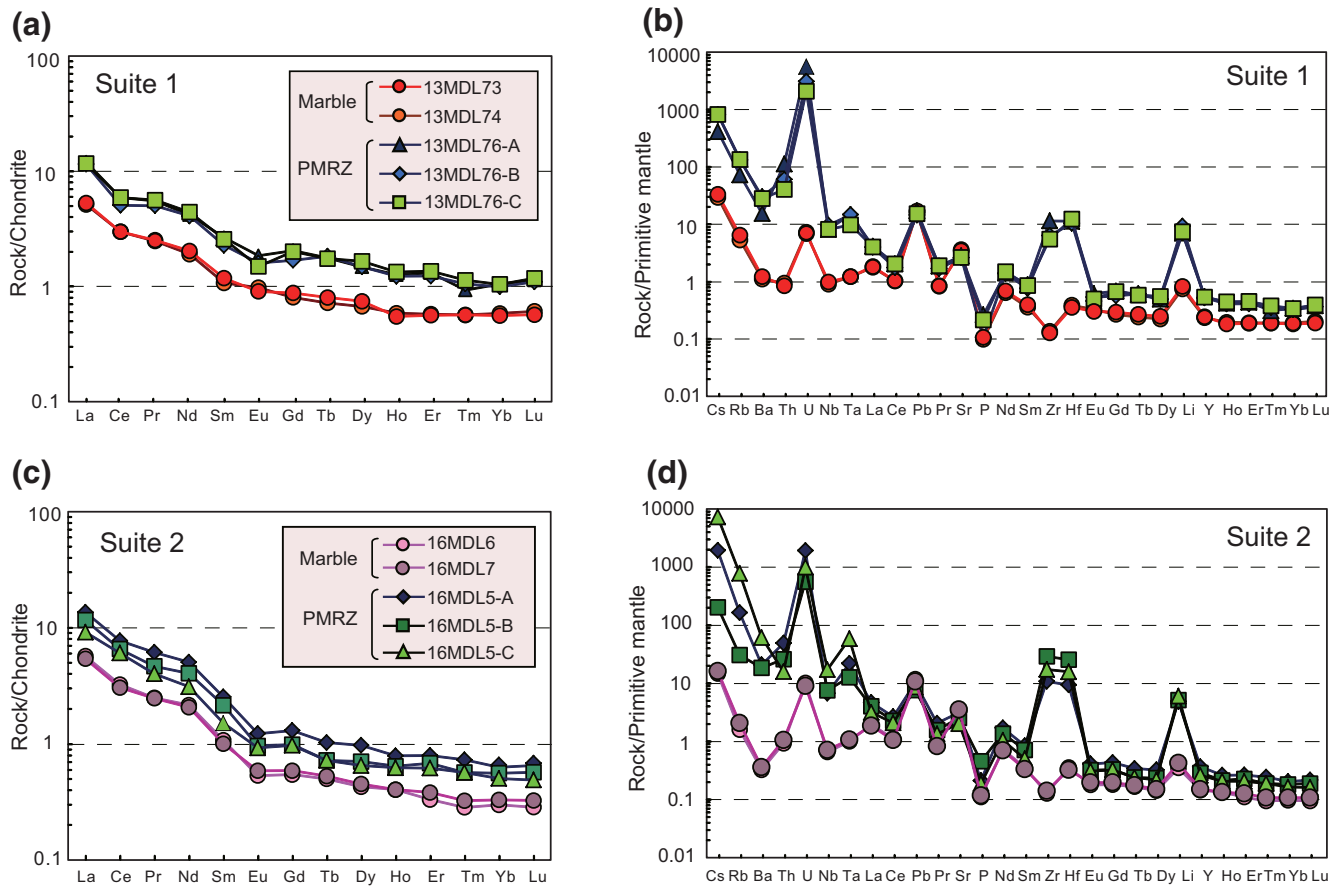


Figure 4. Chondrite-normalized REE diagrams (a) and (c) and primitive mantle-normalized trace element diagrams (b) and (d) of marbles and PMRZs. The normalization values are from Sun and McDonough (1989).

steep light rare earth element (LREE)-enriched pattern in the chondrite-normalized diagrams (Figures 4a and 4c). The marbles also contain considerable amounts of Sr (72–76 $\mu\text{g/g}$, Figures 4b and 4d).

Compared with the marbles, the PMRZ samples have lower contents of CaO (20–25 wt%) and volatiles (17–20 wt%) and higher contents of other major elements. SiO_2 (17–22 wt%), Al_2O_3 (6–14 wt%), Na_2O (0.12–0.84 wt%), TiO_2 (0.15–0.53 wt%), and K_2O (0.18–2.35 wt%) contents of PMRZs are variable, depending on the abundances of silicate/oxide minerals. The PMRZs exhibit a similar LREE-enriched pattern to the marbles (Figures 4a and 4c). However, the rare earth element (REE) contents of the PMRZs are higher than those of the marbles. Moreover, the PMRZs show slightly negative Eu anomalies. High field-strength elements (HFSEs, Nb, Ta, Zr, Hf, and U), Pb, and Li of the PMRZs show positive anomalies in primitive mantle-normalized diagrams (Figures 4b and 4d). The PMRZs have higher contents of large-ion lithophile elements (LILEs), HFSEs, and transition metal elements (TMEs, Cr, V, and Ni) than the marbles.

5.2. Mineral Compositions

The major element and trace element data of minerals are presented in Tables S3 and S4, respectively.

5.2.1. Spinel

Spinel has high Al contents (67–71 wt%) and X_{Mg} values [$= \text{Mg}/(\text{Mg} + \text{Fe}^{2+}) = 0.97\text{--}0.98$]. The Cr_2O_3 contents range from 0.6 to 3.0 wt%. Analyses of X-ray maps on a representative spinel porphyroblast indicate that this mineral exhibits distinct core–rim compositional zoning (Figures 5a–5d). The cores of spinel generally have higher Cr# [$= \text{Cr}/(\text{Cr} + \text{Al})$ molar] values (0.02–0.04) and Cr contents (10,000–15,000 $\mu\text{g/g}$)

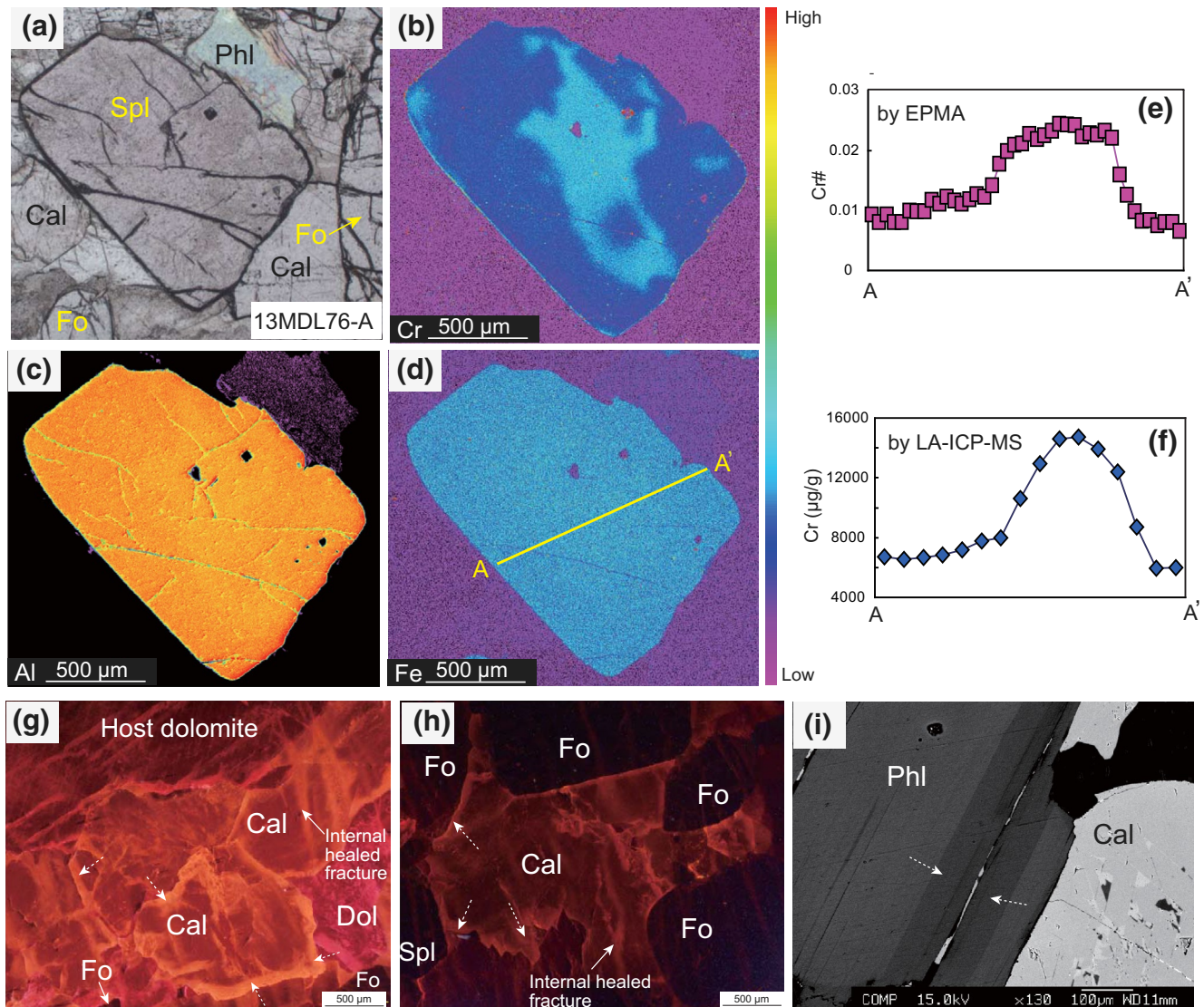


Figure 5. Mineral compositional zoning of spinel, calcite, and phlogopite from the PMRZ sample 13MDL76-A. (a) Photomicrograph of a representative spinel in textural equilibrium with phlogopite, calcite, and forsterite. (b) X-ray map of Cr. (c) X-ray map of Al. (d) X-ray map of Fe. (e) Variation in Cr# [= Cr/(Cr + Al)] along a rim-core-rim profile (by EPMA). (f) Variation in Cr content along a rim-core-rim profile (by LA-ICP-MS). The profile location is shown in (d). (g), (h) CL images showing the core-rim zoning (with a brighter rim) of calcite. Note that some thin bright bands through the interior of calcite crystal are consistent with healed fractures along which the reactive fluids once passed. (i) BSE image showing the core-rim zoning (with a darker rim) of phlogopite. The rims of calcite and phlogopite are indicated by the dotted arrows in (g)–(i).

than the rims (0.005–0.01 for Cr# and 1,000–7,000 $\mu\text{g/g}$ for Cr contents) (Figures 5e and 5f). The V (600–830 $\mu\text{g/g}$), Zn (500–820 $\mu\text{g/g}$), Ni (70–120 $\mu\text{g/g}$), and Ga (85–110 $\mu\text{g/g}$) contents of cores and rims are similar.

5.2.2. Forsterite

Both forsterite inclusions and matrix forsterite have endmember compositions of $X_{\text{Mg}} = 0.99$. Forsterite has low contents of Ni (16–34 $\mu\text{g/g}$), Mn (50–57 $\mu\text{g/g}$), and P (35–84 $\mu\text{g/g}$) and elevated contents of Ca (100–360 $\mu\text{g/g}$) and Li (7–14 $\mu\text{g/g}$). Al and Cr contents range from 17 to 61 $\mu\text{g/g}$ and from 1.1 to 5.4 $\mu\text{g/g}$, respectively. The contents of most REEs, LILEs, and HFSEs in forsterite are below the detection limit.

5.2.3. Dolomite and Calcite

Dolomite in host marbles has near endmember compositions, with very low Fe contents of 0.001–0.003 apfu (Figure S1a). Dolomite has Sr contents of 64–85 $\mu\text{g/g}$, Mn contents of 30–50 $\mu\text{g/g}$, and Y contents of 1.2–

10 $\mu\text{g/g}$, and exhibits an LREE-enriched pattern (Figures S1b–S1d). Rare PMRZ dolomite has a similar composition to dolomite in host marbles.

Both calcite inclusions in spinel or forsterite and matrix calcite in the PMRZs are simple solid solutions between calcite and dolomite with Fe contents of 0.002 apfu (Figure S1a) and MnO contents of 0–0.06 wt%. Calcite inclusions are compositionally homogeneous and have high MgO contents of 4.7–5.6 wt% (Mg/Ca ratio \sim 0.13–0.15). In contrast, matrix calcite has an obvious variation in MgO contents (1.9–4.2 wt%) and Mg/Ca ratios (0.05–0.11). Matrix calcite exhibits pronounced zoning in cathodoluminescence (CL) images with brighter rims (Figures 5g and 5h), indicating a fluid-assisted replacement process. Moreover, thin bright bands through the interior of calcite are observed (Figures 5g and 5h); this characteristic is consistent with a healed fracture along which reactive fluid once passed (Putnis & Austrheim, 2010). All the textures above indicate the existence of dissolution–precipitation processes after the formation of calcite (Putnis, 2009; Putnis & Austrheim, 2010). The brighter rims have higher Mn contents (225–330 $\mu\text{g/g}$) than the cores (25–29 $\mu\text{g/g}$) (Figure S1b). Calcite has higher Sr, Pb, and REE contents than dolomite. All types of calcite show a similar LREE-enriched pattern with negative Eu anomalies (Figure S1d).

5.2.4. Phlogopite

Phlogopite has near-Mg endmember composition ($X_{\text{Mg}} \sim 0.99$ –1) and is enriched in F (1.5–1.9 wt%) (Figure S2a). The TiO_2 contents range from 0.6 to 1.6 wt% (Figure S2b). Phlogopite has high K (0.63–0.88 apfu) and Na (0.10–0.39 apfu) contents and low Ca contents (<0.01 apfu). Some matrix phlogopite grains show a compositional zonation in back-scattered electron (BSE) images with darker rims. The rims have lower Na, Fe, and Ti contents (Figures 5i, S2b, and S2c). Phlogopite has high contents of Cs (19–80 $\mu\text{g/g}$), Ba (315–1350 $\mu\text{g/g}$), Rb (400–660 $\mu\text{g/g}$), and Li (14–40 $\mu\text{g/g}$) (Figure S2d). In addition, it contains considerable amounts of Nb (11–26 $\mu\text{g/g}$) and Zr (1–16 $\mu\text{g/g}$). The contents of REEs, Th, and U are typically low.

5.2.5. Geikielite

Geikielite is composed of 86–91 mol% geikielite and 9–14 mol% ilmenite components. The MnO content of geikielite is lower than 0.1 wt%.

5.3. Textures, Inclusions, and U–Pb Ages of Baddeleyite and Zircon

Baddeleyite in the PMRZs is light brownish to yellowish, prismatic or round, and up to 800 μm in its longest dimension (Figures 6a and 6b). In CL images, most baddeleyite grains display zoning with dark chaotic or cloudy cores and bright homogeneous rims, suggesting at least two stages of mineral growth (or recrystallization) (Rubatto & Scambelluri, 2003). Moreover, in some baddeleyite grains, bright veinlets are found to extend from the rims into the regions of cores (Figure 6c). Baddeleyite contains inclusions of spinel, forsterite, phlogopite, and calcite (Figures 6a and 6b), which indicates that baddeleyite formed by the metasomatism rather than being derived by physical transfer along with the fluids.

The U–Th–Pb isotopic results of baddeleyite are presented in Table S5 and shown in Figures 7a and 7b. The measured $^{206}\text{Pb}/^{204}\text{Pb}$ ratios of all analyses are higher than 15,000, indicating very low proportions of common Pb. Sixteen analyses on the baddeleyite cores of sample 13MDL76-A gave U contents of 1,675–2,789 $\mu\text{g/g}$ and Th/U ratios of 0.001–0.002. In the Tera–Wasserburg concordia diagram, all uncorrected analyses define a regression line with a lower intercept age of 35.77 ± 0.81 Ma (Figure 7a). Ten analyses on the 13MDL76-A baddeleyite rims gave lower U contents of 1,256–2,147 $\mu\text{g/g}$ (Th/U ratios of 0.001) and a lower intercept age of 23.03 ± 0.44 Ma. The U contents (and Th/U ratios) of the 16MDL5-A baddeleyite cores and rims are similar to those of the 13MDL76-A baddeleyite cores and rims, respectively. Twenty analyses on the 16MDL5-A baddeleyite cores and nine analyses on the rims yielded lower intercept ages of 35.16 ± 0.52 and 24.12 ± 0.99 Ma, respectively (Figure 7b).

Zircon mainly occurs as reaction rims that partially replace baddeleyite (Figure 6d). Most of the zircon reaction rims are not large enough for ion beam spot analyses. Rare individual zircon grains were recovered from sample 13MDL76-A. The occurrence of calcite, forsterite, and phlogopite inclusions indicates that the host zircon crystallized during the metasomatism (Figure 6e) and rule out the possibility that they were mechanically mixed from external sources. Five analyses of zircon gave U contents of 1766–4134 $\mu\text{g/g}$ and

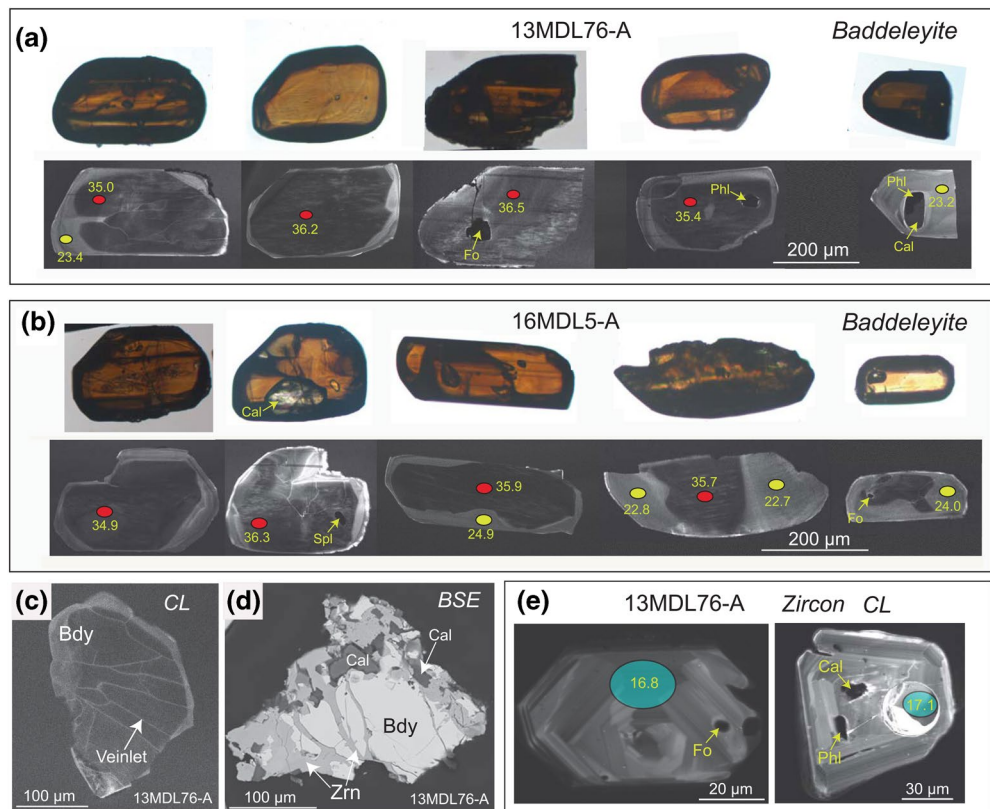


Figure 6. Textures and inclusions of baddeleyite and zircon in the PMRZs. (a) Representative microphotographs (in plane-polarized light) and corresponding CL images of baddeleyite in sample 13MDL76-A. (b) Representative microphotographs and corresponding CL images of baddeleyite in sample 16MDL5-A. Inclusions of spinel, forsterite, phlogopite, and calcite are found in baddeleyite. (c) A CL image showing bright veinlets extending from the rims to cores of baddeleyite in sample 13MDL76-A (the veinlets are still baddeleyite). (d) A BSE image showing the partial replacement of baddeleyite by zircon in sample 13MDL76-A. (e) Representative CL images of zircon in sample 13MDL76-A. The red, yellow, and blue circles in CL images represent the locations of SIMS analyses. The numbers near the circles and in the circles represent the ^{207}Pb -corrected $^{206}\text{Pb}/^{238}\text{U}$ ages.

Th/U ratios of 0.039–0.058. The uncorrected analyses define a regression line with a lower intercept age of 17.05 ± 0.27 Ma (Figure 7c).

6. Mass-Balance Calculation and Material Transfer

The differences in mineral assemblage and whole-rock composition between the PMRZs and marbles indicate significant material exchange during the metasomatism. In particular, the replacement of dolomite by silicate/oxide minerals is accompanied by CO_2 losses. Therefore, a mass-balance calculation was conducted to assess the chemical feedback of fluid metasomatism. The calculation can examine whether the change in element concentration is due to scavenging or dilution and provide quantitative estimations on time-integrated mass transfer (the percent of losses or gains for mobile elements during metasomatism).

The mass transfer (τ_m) of any mobile element m during metasomatism from an original sample O to a metasomatized sample A can be calculated by the following equation (Ague & van Haren, 1996; Guo et al., 2009):

$$\tau_m = \Delta M_m^{O-A} / M_m^O = \left(C_m^A / C_m^O \right) \left(C_i^O / C_i^A \right) - 1$$

where ΔM_m^{O-A} is the mass change of m during metasomatism; M_m^O is the mass of m in sample O; C_m^A and C_i^A are the concentrations of m and the most immobile element i in sample A, respectively; and C_m^O and C_i^O are the concentrations of m and i in sample O, respectively.

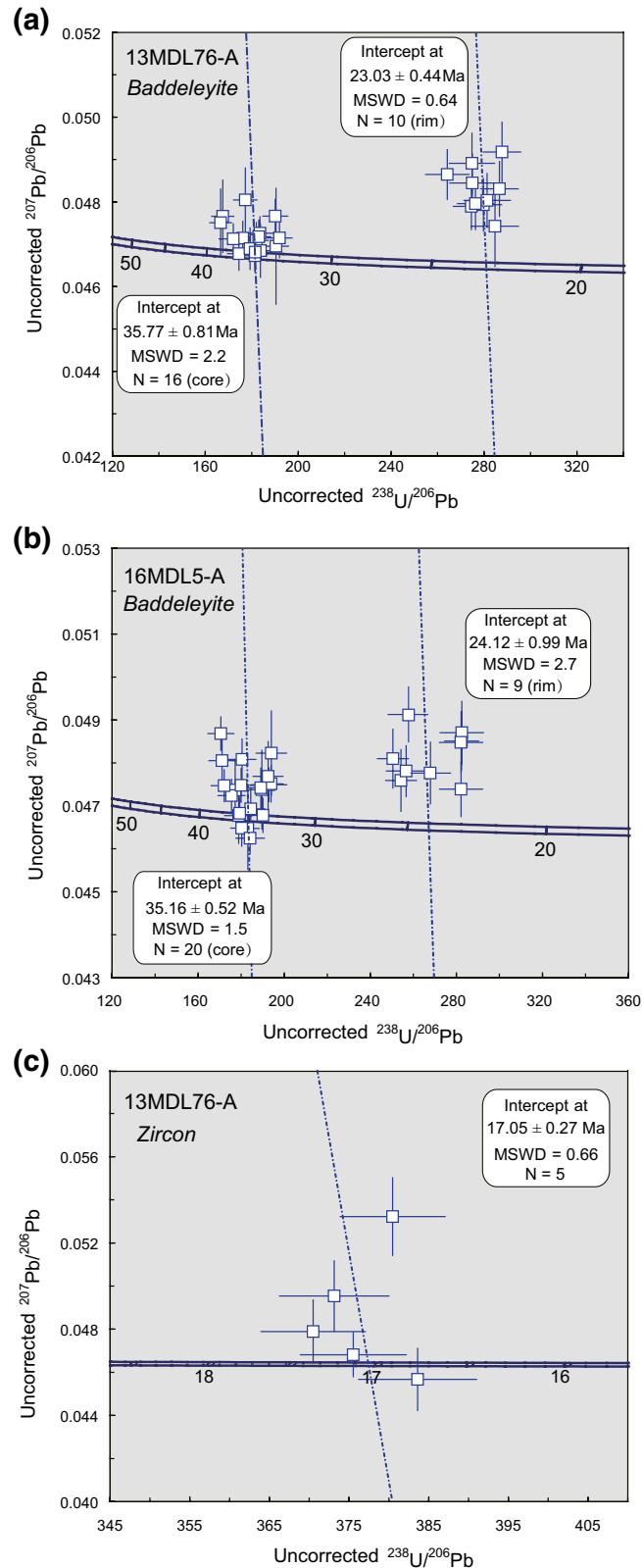


Figure 7. Tera-Wasserburg U–Pb concordia diagrams for baddeleyite from samples 13MDL76-A (a) and 16MDL5-A (b) and zircon from sample 13MDL76-A (c). Data-point error bars are 1σ . Weighted age uncertainties are at 95% confidence level.

The average composition of marbles 13MDL73 and 13MDL74 was used as the unaltered reference for the PMRZ samples of Suite 1, and the average composition of marbles 16MDL6 and 16MDL7 was used as the reference for the PMRZ samples of Suite 2. Ytterbium (Yb) was chosen as the most immobile element due to following considerations: (1) the host marbles and PMRZs have a similar REE pattern (Figures 4a and 4c). This result indicates that REEs are not significantly mobile during the metasomatism (Ague, 2017; Penniston-Dorland & Ferry, 2008), because a strong fractionation of LREE from HREE in the metasomatized products is expected if the reactive fluids mobilized REEs; (2) both the experimental and natural investigations indicate that Yb generally has a lower mobility than other REEs in aqueous fluids (e.g., Guo et al., 2015; Kessel et al., 2005); (3) all of other potential elements with low solubilities in fluids, such as HFSEs, are inappropriate for the use as the immobile element(s) because of the occurrence of many Ti-rich and Zr-rich phases in the metasomatic PMRZs (Figures 3g, 3h, and 6). Uncertainty estimation and error propagation followed the procedure of Guo et al. (2019). The calculated mass gains or losses are presented in Table S6 and Figures 8a and 8b.

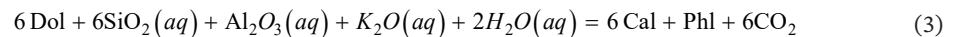
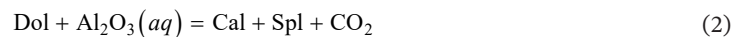
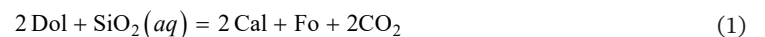
The results indicate that both suites of PMRZs have similar mass transfer characteristics. All of REEs exhibit minor mass transfer (mostly $< \pm 30\%$). The large mass gains ($> +260\%$) of Si, Al, Ti, K, and Na in the PMRZs are attributed to the growth of the silicate and oxide minerals (forsterite, phlogopite, spinel, and geikielite). LILEs (Cs, Rb, and Ba) and Li show significant mass gains ($> +380\%$), which are mainly controlled by the growth of phlogopite. The enrichments ($> +370\%$) of HFSEs (Nb, Ta, Zr, Hf, Th, and U) are dominated by the formation of Ti-rich and Zr-rich accessory phases (geikielite, rutile, baddeleyite, and zircon) and the enrichments ($> +560\%$) of TMEs (Cr, V, and Ni) are ascribed to the growth of spinel. In contrast, CO_2 and Ca were obviously removed from the marble system during the formation of PMRZs (from -78 ± 2 to $-81 \pm 2\%$ and from -56 ± 4 to $-62 \pm 4\%$, respectively). In addition, Mg and Sc show low mass losses ($< -32\%$) during the metasomatism.

7. Discussion

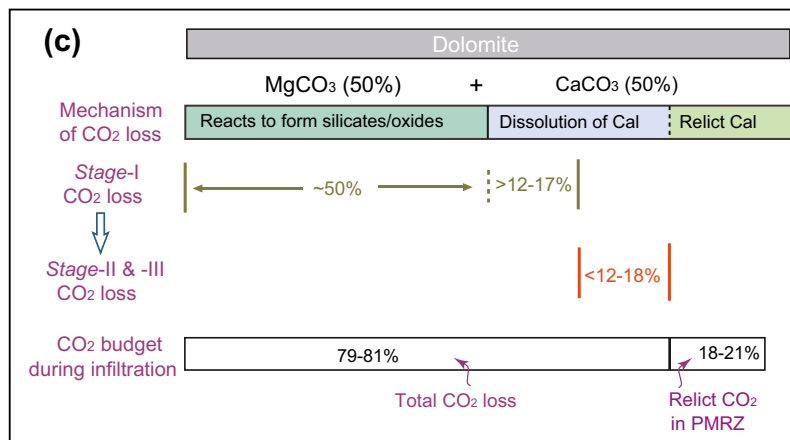
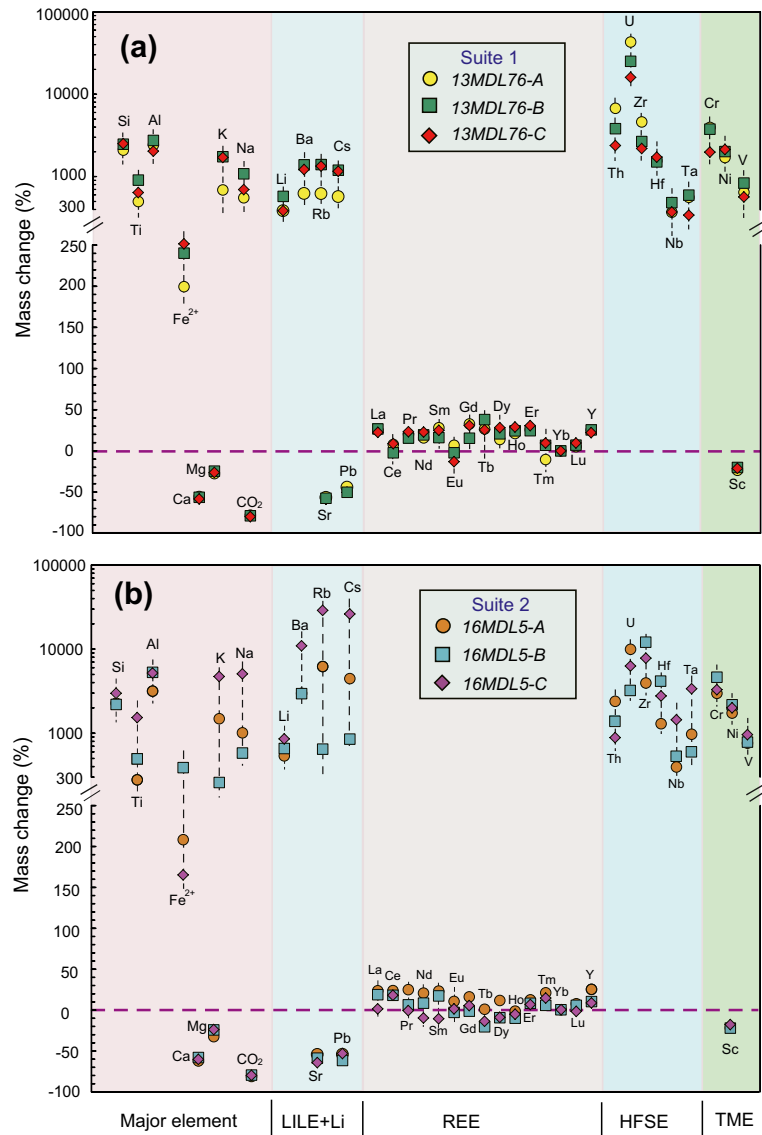
7.1. Multiple Episodes of Fluid Infiltration During the Formation of PMRZs

Both field and petrological evidence indicate that the PMRZs represent fossil flow channels of externally infiltrating fluids in the marbles. The textural and compositional features of metasomatic minerals provide a key record of fluid evolution processes (e.g., Barker et al., 2006; Bégué et al., 2019; Jamtveit et al., 1992). Although no symmetrical sequences of mineral zones are found in the PMRZs, the zoning of metasomatic minerals (spinel, baddeleyite, phlogopite, and calcite, Figures 5 and 6) and the replacement textures of baddeleyite by zircon (Figure 6d), as well as baddeleyite/zircon U–Pb chronology (Figure 7), clearly indicate that the formation of the PMRZs involves multiple stages of fluid-assisted mineral growth.

The initial fluid infiltration (Stage-I) led to the growth of most minerals in the PMRZs (i.e., the cores of metasomatic minerals) according to the following reactions:



The temperature (T) of Stage-I infiltration was determined by calcite–dolomite solvus thermometry (Anovitz & Essene, 1987). The homogeneous calcite inclusions in spinel and forsterite were used for the calculations because they provide more accurate estimates of peak- T conditions compared to the matrix calcite (Ferry, 2001). The calculations for different PMRZ samples yielded a same temperature range of 704–750°C (Table S3). The pressure of Stage-I infiltration is estimated to be close to the peak metamorphic pressure (~ 8 kbar, Thu & Enami, 2018) of spinel-forsterite-bearing marbles nearest to the studied outcrop (in the Thabeikgyin area, Figure 1a). In situ U–Pb dating on the baddeleyite cores, which contain forsterite, spinel,



and phlogopite inclusions, indicates that the Stage-I metasomatism occurred at ~35–36 Ma (Figures 7a and 7b). The ages of Stage-I infiltration are similar to the emplacement ages of nearby hornblende syenites (33.11 ± 0.93 to 30.90 ± 0.64 Ma; Barley et al., 2003). We suggest that the Stage-I infiltrating fluid most likely is related to the syenite magmatic event.

The formation of rims of spinel, baddeleyite, and phlogopite demonstrates a later generation of mineral reaction (Stage-II) in the PMRZs by either the infiltration of an external fluid or the metamorphism in a closed system (e.g., Stewart & Ague, 2018). The distinctive core–rim zoning of these minerals is consistent with a replacement process via an interface-coupled dissolution–precipitation (ICDP) mechanism (e.g., Putnis, 2009; Putnis & Austrheim, 2010). This interpretation is strengthened by the occurrence of irregular veinlets extending from the baddeleyite rims to cores, indicating that the crystallization of rims is related to a reactive fluid influx (Figure 6c). The sole hydrous mineral in the PMRZs is phlogopite and no breakdown texture of this mineral is found at Stage-II. Therefore, no mineral can provide the H₂O-rich fluids for the ICDP process if the system is closed. This result indicates that the formation of rims of PMRZ minerals is induced by a fluid infiltration event (Stage-II infiltration). The lower Cr contents of the spinel rims and lower U and Pb contents of the baddeleyite rims compared to their cores demonstrate the mobilization of these elements during the Stage-II infiltration. The baddeleyite rims yielded ages of ~23–24 Ma (Figures 7a and 7b), which represent the time of Stage-II infiltration. Fluid source and P–T conditions of this infiltration episode are difficult to be precisely constrained due to a lack of corresponding fluid events in the studied area and of appropriate thermobarometers. However, the mineral assemblage of Stage-II is the same as that of Stage-I, implying a similar nature for the two stages of fluids. It is therefore reasonable to consider that the P–T conditions of Stage-II infiltration are similar to or slightly lower than those of Stage-I infiltration.

The final episode of mineral growth (Stage-III) is characterized by the partial replacement of zoned baddeleyite by zircon, representing a new ICDP process in the presence of a fluid postdating Stage-II infiltration. The reaction can be written as follows:



This reaction requires the addition of SiO₂, which might be derived from either an infiltrating fluid or the breakdown of silicate minerals in a closed system at the Stage-III (e.g., Zhou et al., 2020). The only two silicate minerals in the PMRZs are forsterite and phlogopite. Both minerals are stable at the Stage-III and no breakdown textures are observed for both of them (Figures 3c–3f). These observations indicate that both minerals cannot provide SiO₂ for the formation of zircon. Therefore, the added SiO₂ is externally derived and the Stage-III reaction is caused by the fluid infiltration rather than the “closed-system” metamorphism. Moreover, the replacement of geikielite by rutile (Figure 3g) may also occur at this stage, if the growth of rutile had not taken place in the previous stage. The U–Pb dating of individual zircon grains, which contain forsterite, calcite, and phlogopite inclusions, indicates that the Stage-III infiltration occurred at ~17 Ma (Figure 7c). This infiltration episode coincides well with the emplacement of a nearby granite dyke (17.0 ± 0.3 Ma) that might be related to the anatexis of surrounding gneisses (Mitchell et al., 2012). The peak metamorphic conditions of the gneisses are ~5 kbar and 680°C (Searle et al., 2007), which represent a best estimate of conditions for the Stage-III metasomatism.

In summary, the above results demonstrate that the PMRZs formed by three episodes of fluid infiltration into the marbles at time intervals of ~7–13 Ma rather than the closed-system metamorphic evolution. Moreover, it is indicated that the Stage-II and Stage-III fluids went through the marbles along the same channels

Figure 8. Mass-transfer diagrams (a), (b) and sketch map (c) of CO₂ release during the metasomatism of dolomite marbles. (a) The mass losses and gains of different groups of elements for the PMRZs from the Suite 1. (b) The mass losses and gains of different groups of elements for the PMRZs from the Suite 2. The mass transfer was calculated relative to the average composition of host marbles. Ytterbium (Yb) was chosen as the most immobile element. A positive deviation from the 0% reference line (horizontal dashed lines) indicates mass gain, whereas a negative deviation indicates mass loss of a certain element. (c) A sketch showing the transfer mechanism and amount of CO₂ removal at different stages of fluid infiltration. The CO₂ loss at the Stage-I is larger than 62–67% (~50% by the breakdown reactions of MgCO₃ and >12–17% by the calcite dissolution). The sum of CO₂ losses at the Stage-II and Stage-III is lower than 12–18%. The total CO₂ loss during the multiple episodes of infiltration is ~79–81% and ~18–21% CO₂ is still remained in the PMRZs. For details, see the text.

as the Stage-I fluid. The formation of metasomatic minerals in the PMRZs mostly occurred at the first stage, whereas later episodes of fluids only modified the product minerals of Stage-I via an ICDP mechanism.

7.2. Thermodynamic Constraints on Fluid-Mineral Equilibria and Fluid Composition

The growth of metasomatic minerals in carbonates is controlled by the compositions of fluid and fluid-mineral equilibria at specific P–T conditions (e.g., Ague, 2014; Bégué et al., 2019; Ferry, 1994). To understand the phase relationships and quantify the fluid chemistry evolution over the whole metasomatic process, diagrams of activity (SiO_2 and TiO_2) vs. X_{CO_2} [= $\text{CO}_2/(\text{CO}_2 + \text{H}_2\text{O})$] for the PMRZs at inferred P–T conditions (8 kbar and 730°C for Stage-I and Stage-II; 5 kbar and 680°C for Stage-III) were calculated using the internally consistent thermodynamic dataset (Holland & Powell, 1998), a MATLAB-based code package (Chu & Ague, 2013), and updated activity models (Fo and Dol from Holland and Powell (1998); Di from Green et al. (2007); Gk from Ghiorso and Evans (2008); H_2O – CO_2 fluid from Holland and Powell (2003)). The activities of endmembers were calculated based on mineral compositions (Cal, Bdy, Zrn, and Rt were treated as pure endmembers). The calculated results are shown in Figure 9.

Reaction (1) involves the addition of SiO_2 in the dolomite and the formation of calcite and forsterite. Moreover, diopside, which has higher Si concentrations than forsterite, is absent in the assemblages of all metasomatic stages, indicating that SiO_2 activities in the fluids do not suffice the following reaction:



In combination with the presence of baddeleyite rather than zircon, low X_{CO_2} (<0.1) and a_{SiO_2} (<0.14) conditions are required for the Stage-I and Stage-II fluids (Figure 9a). The coexistence of geikielite + calcite in the PMRZs (reaction 4) further indicates that X_{CO_2} should be lower than 0.08 (Figure 9b), which places a_{SiO_2} of the Stage-I and Stage-II fluids to be <0.12 (blue line in Figure 9a). The same calculations were performed for the Stage-III metasomatism in terms of inferred conditions. The assemblage of geikielite + rutile + calcite allows X_{CO_2} of the Stage-III fluid to be <0.19 (Figure 9b). The partial replacement of baddeleyite by zircon indicates that a_{SiO_2} of the Stage-III fluid is buffered at a value of 0.15 by reaction (5). These results, together with the absence of diopside, yielded a range of fluid X_{CO_2} of 0.08–0.19 for the Stage-III assemblage (blue line in Figure 9c). Therefore, the Stage-III reactive fluid has higher X_{CO_2} and a_{SiO_2} than the earlier two stages of fluids. Moreover, rock buffering the a_{SiO_2} of the fluid implies a relatively low fluid/rock ratio at the Stage-III. This is consistent with the petrologic observations, which show that only a small portion of baddeleyite is partially replaced by zircon at the Stage-III (Figures 3h, 6a, 6b, and 6d).

7.3. Permeability Evolution and Multiple-Stage Fluid Flow Pattern

The most prominent characteristic of metasomatism in the PMRZs is that three episodes of fluids, regardless of their fluxes and chemical compositions, flowed along the same pathways. Permeability is a principal parameter determining how readily a fluid can flow through the rock medium and therefore controls the spatial pattern of fluid flow and the metasomatic reaction progress (e.g., Ague, 2014; Cartwright, 1997; Cox, 2007; Yardley & Balashov, 1998). It is widely accepted that the permeability, which strongly (often cubic) depends on rock porosity, changes over time (Bickle & Baker, 1990; Connolly, 1997). Therefore, permeability evolution during multiple episodes of infiltration is discussed in this section.

The protolith marbles (pure dolomite before the infiltration) are essentially impermeable (e.g., porosity $\sim 10^{-6}$, Bickle & Baker, 1990) (Figure 10a). However, rare micro-fractures or micro-cracks, which are generated by deformation, faulting, or seismicity, might locally exist and form heterogeneous porosity fields. These fields could have a slightly higher permeability (φ_{initial} , Figure 10b) than the host marbles (e.g., Baumgartner et al., 1997; Bucher-Nurminen, 1989; Holness, 1997; Jamtveit et al., 2019). The Stage-I fluid may infiltrate along the initial micro-fractures and induce decarbonation reactions in the regions where the fluid passed through (Figure 10a). The reactions caused the overall solid volume to shrink. For example, the reaction (1) can lead to a decrease of $\sim 9\%$ in volume, which produced a larger porosity and a higher permeability environment (e.g., Baumgartner et al., 1997; Bégué et al., 2019). The enhanced permeability facilitates further fluid flow at the Stage-I, leading to positive feedback between the reactions and fluid influx.

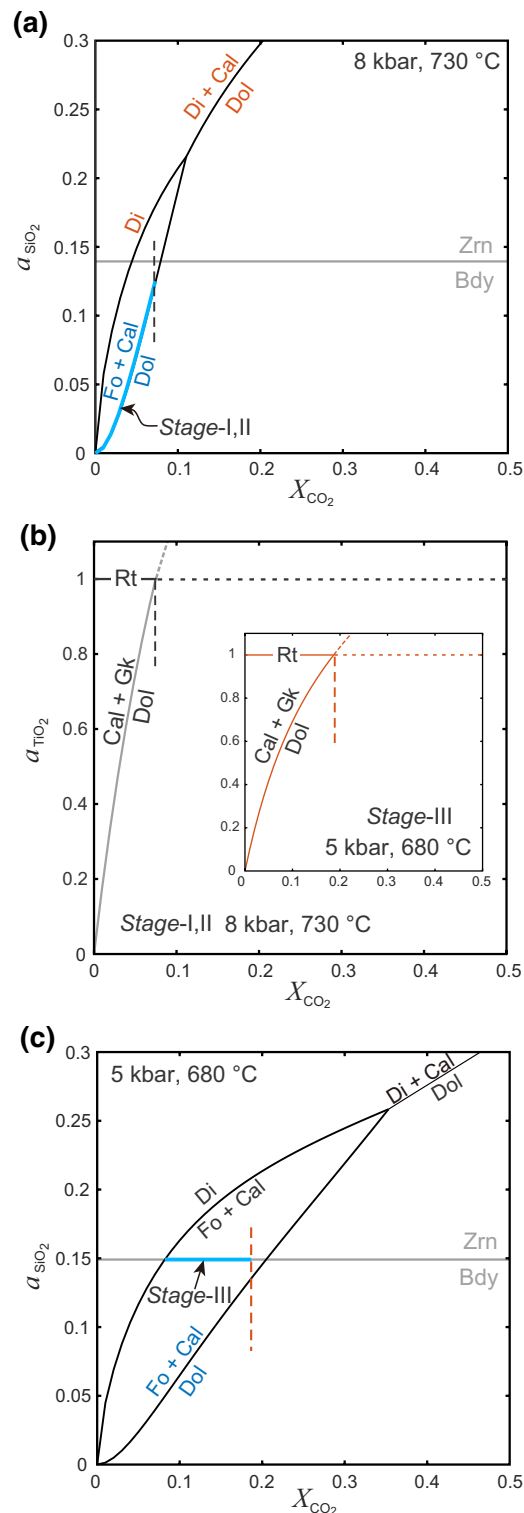


Figure 9. Calculated diagrams of component activity (a) vs. X_{CO_2} [= $CO_2/(CO_2 + H_2O)$] showing fluid-mineral equilibria during the metasomatic formation of PMRZs. Each diagram is drawn with fluid presence. (a) Diagram of a_{SiO_2} vs. X_{CO_2} at 8 kbar and 730°C (conditions of the Stage-I and Stage-II fluid infiltration). The blue line denotes the compositional range of the Stage-I and Stage-II fluids. (b) Diagrams of a_{TiO_2} vs. X_{CO_2} at 8 kbar and 730°C and 5 kbar and 680°C (conditions of the Stage-III infiltration, insert figure), respectively. (c) Diagram of a_{SiO_2} vs. X_{CO_2} at 5 kbar and 680°C. The blue line denotes the compositional range of the Stage-III fluid. The orange dashed line, which is used to constrain the upper limit of X_{CO_2} , is derived from the insert of Figure 9b.

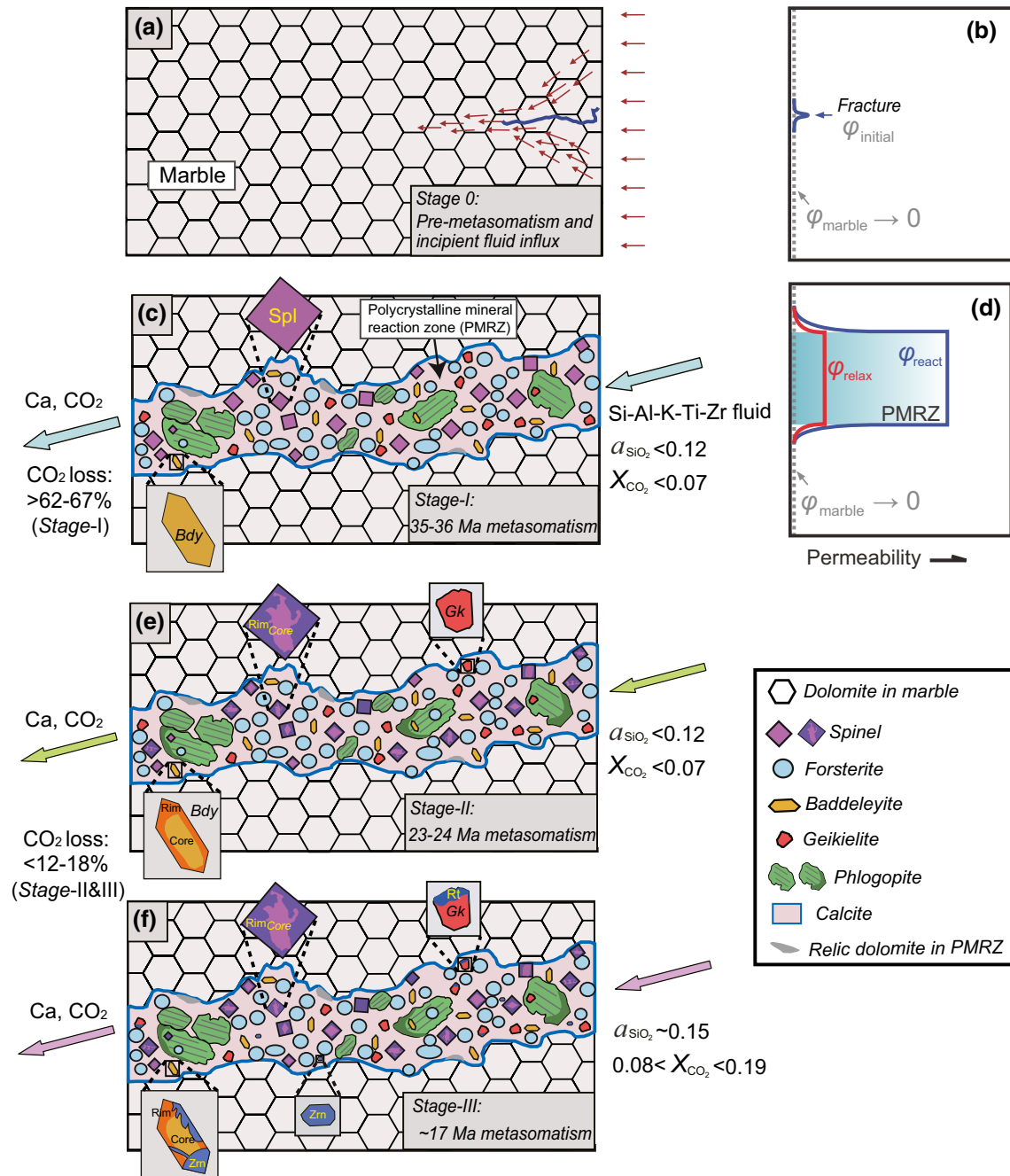


Figure 10. Schematic sketch showing the fluid infiltration history and permeability evolution of the PMRZs in the MMB marbles. (a) Stage-0: Pure dolomite marbles with rare fractures (blue region). (b) The fracture region has a slightly higher permeability ($\phi_{initial}$) than the marble (essentially impermeable), which allows the influx of incipient fluid along this region. (c) Stage-I: The first episode of fluid infiltration and metasomatism at $\sim 35\text{--}36$ Ma. This process formed most of metasomatic minerals (Fo, Spl, Phl, Bdy, Gk, and Cal) in the PMRZs. Most dolomite in the PMRZs has been consumed at this stage. This process led to a large amount of CO_2 loss by both the decarbonation reactions and calcite dissolution. (d) The Stage-I metasomatic process produced a higher permeability (ϕ_{react}) in the PMRZs. After the Stage-I fluid drainage, the high permeability of PMRZs may be reduced with time by pore space collapse at a relatively high pressure of ~ 8 kbar. However, the formation of deformation-resistant minerals (Spl and Fo) can help prevent the full collapse of pore network and maintain a still higher permeability (ϕ_{relax}) in the PMRZs than in the impermeable marble. (e) Stage-II: The second episode of fluid infiltrated along the previous pathway at $\sim 23\text{--}24$ Ma. This process modified the composition of preexisting minerals by an ICDP mechanism (formation of the rims of minerals). (f) Stage-III: The final episode of fluid infiltration occurred at ~ 17 Ma, which is recorded by the replacement of baddeleyite by zircon and the replacement of geikielite by rutile. Episodes of Stage-II and Stage-III infiltration resulted in limited amounts of CO_2 transfer.

Consequently, the decimeter-wide reaction zones formed along with the penetration of Stage-I fluid (Figure 10c). These reaction zones have a much higher permeability (φ_{react}) than the host marbles (Figure 10d; Zhang et al., 1994, 2000).

After the Stage-I metasomatism, the pore space in the PMRZs may readily collapse due to the fluid drainage at relatively high pressure conditions (~ 8 kbar at the Stage-I and Stage-II) (e.g., Yardley & Balashov, 1998; Zhang et al., 1994, 2000). This compaction process will lead to a decrease in the permeability of the PMRZs with time (e.g., decreased from φ_{react} to φ_{relax} , Figure 10d) (Baumgartner et al., 1997; Zhang et al., 1994, 2000). However, the formation of high abundances of deformation-resistant minerals, such as spinel and forsterite (33–54 vol.%), can prevent the full collapse of pore network and maintain a still higher permeability (φ_{relax}) in the PMRZs than in the impermeable marbles after the Stage-I metasomatism (Figure 10d) (Baumgartner et al., 1997). This condition of permeability allows the subsequent Stage-II fluid (23–24 Ma, Figure 10e) and Stage-III fluid (~ 17 Ma, Figure 10f) to flow along the pathways created by the Stage-I fluid (~ 35 – 36 Ma).

This fluid flow behavior exerts important influences on the metasomatism and mass transfer in marbles during orogenic metamorphism. Because the reaction zone generated by early-stage fluid influx acts as a favorable channel for the influxes of subsequent fluids, focused flow will dominate over pervasive flow through the marbles. This leaves the marbles (excluding the fluid flow channels) largely intact during repeated episodes of infiltration and the mass transfer is confined into narrow zones. The reaction zones may involve multiple infiltration processes of chemically distinct fluids. In the present study, we were able to distinguish these events by the fortuitous crystallization of datable minerals, but more commonly this might not be the case. Consequently, care should be taken in the interpretation of textural and geochemical results of reaction zones in marbles in future studies, as they may represent a signal acquired during multiple episodes.

7.4. Assessing CO₂ Release During Multiple Episodes of Fluid Infiltration

Both petrologic analyses and mass-balance calculations demonstrate a significant removal of CO₂ (>75%) accompanied by the growth of silicate/oxide minerals. Three episodes of fluid influx are recognized in the PMRZs. It is thus essential to clarify the amounts of released CO₂ during different episodes.

Based on the reactions (1)–(4), the carbon in the MgCO₃ endmember of dolomite is released by the growth of Mg-silicates/oxides, which mainly occurred during the Stage-I infiltration (see section 7.1). Only rare dolomite relics can be found in the PMRZs (<2 vol.%), suggesting that most of the dolomite in these zones has been consumed and thus $\sim 50\%$ CO₂ of the dolomite protolith is released through the decarbonation reactions of MgCO₃ at the Stage-I (Figure 8c). In contrast, due to the absence of Ca-rich silicate/oxide minerals in the PMRZs, it seems that the carbon in the CaCO₃ endmember of dolomite is preserved in the metasomatized product calcite. However, the calculated time-integrated CO₂ losses for all PMRZ samples are obviously larger than 50% (Figures 8a and 8b), indicating that the CO₂ release cannot be solely attributed to the MgCO₃ breakdown. At least a portion of CO₂ removal should be achieved by the dissolution of calcite in reactive fluids (Ague & Nicolescu, 2014; Manning et al., 2013; Chu et al., 2019). This interpretation is also in accordance with the obvious loss of CaO (up to $-62 \pm 4\%$) during the metasomatism. Moreover, the CL textures of the PMRZ matrix calcite (Figures 5g and 5h) also reveal that the calcite has experienced dissolution–precipitation processes after its formation. However, the calcite dissolution may occur at all of the infiltration stages (from Stage-I to Stage-III) and the sequence of calcite dissolution during these infiltration stages is difficult to be reconstructed from the CL textures due to the lack of chronological data of calcite. Further thermodynamic calculations are thus required to quantify the dissolution of calcite at various stages.

The magnitude of calcite dissolution and relevant CO₂ loss depend on fluid flux at specific P–T conditions, which can be inferred by the amount of SiO₂ input. According to fluid–mineral equilibria analyses, the Stage-I infiltrating fluid has a_{SiO_2} of <0.12 (Figure 9a). We adopted the quartz solubility in aqueous fluids to estimate the SiO₂ contents. The solubility of quartz in H₂O is ~ 0.5 molal at the conditions of the Stage-I (Manning, 1994). Therefore, the maximum SiO₂ content in the Stage-I fluid is 0.06 molal (equivalent to $\sim 1.2 \times 10^2$ mol/m³) if Henry's law behavior is assumed. The mass-balance calculations show that the metasomatism demands the introduction of ~ 21 – 30 g SiO₂ into every 100 g dolomite protolith (Table S6; Fig-

ures 8a and 8b), corresponding to $\sim(10\text{--}14) \times 10^3$ mol SiO_2 added to every 1 m^3 dolomite (density = 2.84 g/cm^3). Thus, the formation of PMRZs requires fluid/rock ratios of $\sim 80\text{--}120$ at the Stage-I. The ratios represent a minimum because (1) the maximum a_{SiO_2} of fluid was used for the calculations and (2) when a fluid flows through a rock, only a small proportion of fluid interacts with reactants (e.g., Yardley & Balashov, 1998).

The solubility of calcite in the water is ~ 0.022 molal at the conditions of Stage-I (Caciagli & Manning, 2003). Therefore, the amount of reactive fluid ($m_{\text{SiO}_2} = 0.06$ molal) that transports 1 mol SiO_2 could dissolve 0.367 mol calcite and transfer 0.367 mol CO_2 . Accordingly, the addition of $(10\text{--}14) \times 10^3$ mol SiO_2 will induce the transfer of $\sim(3.7\text{--}5.1) \times 10^3$ mol CO_2 per 1 m^3 rock at the Stage-I, corresponding to $\sim 12\text{--}17\%$ of CO_2 in the dolomite protoliths ($\sim 3.0 \times 10^4$ mol CO_2 per 1 m^3) (Table S6; Figure 8c). The calculated amounts of dissolved CO_2 represent a minimum because the minimum of fluid/rock ratio was used for the calculations (see the above paragraph). The total loss of CO_2 during the Stage-I metasomatism is therefore larger than 62–67% ($\sim 50\%$ by the breakdown reactions of MgCO_3 and $>12\text{--}17\%$ by the calcite dissolution). The time-integrated outputs of CO_2 are 78–81% (Table S6; Figures 8a and 8b), suggesting only $<12\text{--}18\%$ removal of CO_2 during the episodes of Stage-II and Stage-III infiltration, mainly by the calcite dissolution (Figure 8c). The Stage-I infiltration thus contributes $>78\text{--}84\%$ (dividing the Stage-I CO_2 loss by the time-integrated CO_2 loss) to the total carbon loss during the whole infiltration processes (Table S6).

7.5. Implications for Metamorphic CO_2 Release in Orogenic Belts

The metamorphic CO_2 production during active orogenic processes is believed to exert a significant influence on the Earth's carbon cycle, and its relative fluxes vs. the CO_2 fluxes consumed by chemical weathering might be a key control on climate and environmental changes (e.g., Kerrick & Caldeira, 1998; Menzies et al., 2018; Skelton, 2011; Svensen & Jamtveit, 2010). Available studies reveal two main ways of CO_2 liberation during orogenic metamorphism, depending on the nature and composition of carbon-reservoir rocks. For a hydrous, silicate-bearing, carbon-rich metasedimentary (e.g., calc-silicate rocks), the liberation of CO_2 can be triggered by fluid-involving metamorphism in a relatively closed system (Groppo et al., 2013, 2017; Rolfo et al., 2017). The CO_2 -producing reactions involve the consumption of preexisting carbonates and hydrous phases (scapolite, mica, amphibole, and epidote). In the closed systems, the magnitude of CO_2 removal mainly relies on the carbon and water amounts of protolith and on the metamorphic P–T evolution (Groppo et al., 2017).

In contrast, for an anhydrous, silicate-poor system, such as pure marbles from the MMB in this study, significant CO_2 liberation can only be achieved by the infiltration of external fluids/melts in an open environment. This process widely takes place in high-grade metamorphic terranes where both metacarbonate rocks and frequent fluid/melt flow occur, e.g., the contact zones between marbles and intrusions (e.g., Bégué et al., 2019, 2020; Svensen & Jamtveit, 2010) or metacarbonates interbedded with metapelites and metabasites (e.g., Ague, 2000). The loss of CO_2 from marbles is made by either silicate/oxide-forming reactions (e.g., Bégué et al., 2020; Ferry, 2016) or the congruent dissolution of carbonate minerals (e.g., Ague & Nicolescu, 2014). For a single fluid infiltration episode, the magnitude of CO_2 removal is dependent on the composition and time-integrated amount of fluid (e.g., Evans, 2011; Stewart & Ague, 2018). With respect to the multiple pulses of fluid influx that more commonly occur during a prolonged orogenic process, the CO_2 outflux is further influenced by the flow pattern, which significantly controls the geometry and spatial scope of fluid-penetrating regions. However, the flow pathways for episodic fluids (interval time >5 Ma) in natural carbonate rocks remain unclear due to a lack of direct geological records. Our new results provide key petrological evidence that the later-stage fluids would penetrate marbles along the previous pathways created by the first episode of infiltration, probably until a new high-permeability region is generated by another tectonic event. Therefore, such marbles would experience multiple-stage, infiltration-driven decarbonation processes. Moreover, we find that the liberation of CO_2 from the marbles is largely completed ($>78\%$) in the first infiltration episode. Thus, it is indicated that the initial episode of reactive fluid exerts more profound effects in shaping the geometry of metasomatic zones and releasing CO_2 from orogenic marbles.

We consider that both metamorphic CO_2 -producing processes are essential to quantify the orogenic CO_2 outflux. Since infiltration-driven CO_2 transfer is dominantly controlled by ambient conditions and the input fluids whose compositions are spatially and temporally heterogeneous, the estimate of CO_2 outflux in infiltration process is more difficult than for the closed-system decarbonation process. For both processes,

we suggest that the fluid evolution history should be examined and considered in any attempt of estimating metamorphic CO₂ production and evaluating the source-sink budget of carbon during orogenesis.

8. Conclusions

The combination of petrology, geochemistry, and in situ U–Pb geochronology reveals that isolated, vein-like, gem-bearing reaction zones (selvages) in the Mogok marbles formed by repeated episodes of fluid infiltration along single flow channels.

Three episodes of fluid infiltration, each separated by relatively long time intervals of 7–13 Ma, are recognized in a single PMRZ: the initial episode of fluid infiltration occurred at ~35–36 Ma, leading to the growth of most metasomatic minerals at ~704–750°C; the subsequent episode of fluid penetrated the marbles by the same pathways at ~23–24 Ma, and formed the rims of metasomatic minerals by an ICDP process; the final episode of infiltration occurred at ~17 Ma, which mainly induced the replacement of zoned baddeleyite by zircon.

Fluid-mineral phase equilibria modeling indicates that the first and second episodes of infiltration occurred at the fluid conditions of low a_{SiO_2} (<0.12) and X_{CO_2} (<0.07), whereas the third episode of infiltration occurred at the fluid conditions of higher a_{SiO_2} (0.15) and X_{CO_2} (0.08–0.19).

The distinct flow behavior for episodic fluids in marbles might be related to enhanced permeability in metasomatic zones, which are generated by the initial infiltration and the growth of deformation-resistant metasomatic minerals.

Mass-balance calculations coupled with the estimations of calcite dissolution demonstrate that there are significant differences in the amounts of released CO₂ at different infiltration stages. The first-stage infiltration contributes the largest portion of CO₂ removal (>78% accounting for the total carbon losses), whereas the latter two stages of fluids through the same pathway system lead to much less CO₂ release.

The infiltration-driven CO₂ outflux from marbles in orogenic belts strongly depends on the composition and pathways of infiltrating fluids as well as the P–T conditions of interactions. Our findings prove that preexisting pathways in marbles can be used multiple times at different stages during the evolution of an orogeny, implying that no simple link between aqueous fluid production and CO₂ release can be obtained.

Data Availability Statement

The data used in this paper are available in the supporting information and can be found in Zenodo (<https://doi.org/10.5281/zenodo.4274429>).

References

- Ague, J. J. (2000). Release of CO₂ from carbonate rocks during regional metamorphism of lithologically heterogeneous crust. *Geology*, 28(12), 1123–1126. [https://doi.org/10.1130/0091-7613\(2000\)282.0.CO;2](https://doi.org/10.1130/0091-7613(2000)282.0.CO;2)
- Ague, J. J. (2014). Fluid flow in the deep crust. In K. Turekian & H. Holland (Eds.), *Treatise on Geochemistry* (2nd ed., pp. 203–247). New York, NY: Elsevier.
- Ague, J. J. (2017). Element mobility during regional metamorphism in crustal and subduction zone environments with a focus on the rare earth elements (REE). *American Mineralogist*, 102(9), 1796–1821. <https://doi.org/10.2138/am-2017-6130>
- Ague, J. J., & Nicolescu, S. (2014). Carbon dioxide released from subduction zones by fluid-mediated reactions. *Nature Geoscience*, 7(5), 355–360. <https://doi.org/10.1038/ngeo2143>
- Ague, J. J., & van Haren, J. L. M. (1996). Assessing metasomatic mass and volume changes using the bootstrap, with application to deep crustal hydrothermal alteration of marble. *Economic Geology*, 91(7), 1169–1182. <https://doi.org/10.2113/gsecongeo.91.7.1169>
- Anovitz, L. M., & Essene, E. J. (1987). Phase equilibria in the system CaCO₃–MgCO₃–FeCO₃. *Journal of Petrology*, 28(2), 389–415. <https://doi.org/10.1093/petrology/28.2.389>
- Barker, S. L., Cox, S. F., Eggins, S. M., & Gagan, M. K. (2006). Microchemical evidence for episodic growth of antitaxial veins during fracture-controlled fluid flow. *Earth and Planetary Science Letters*, 250(1–2), 331–344. <https://doi.org/10.1016/j.epsl.2006.07.051>
- Barley, M. E., Doyle, M. G., Zaw, K., Pickard, A. L., & Rak, P. (2003). Jurassic–Miocene magmatism and metamorphism in the Mogok metamorphic belt and the India–Eurasia collision in Myanmar. *Tectonics*, 22(3), 1–11. <https://doi.org/10.1029/2002TC001398>
- Baumgartner, L. P., & Ferry, J. M. (1991). A model for coupled fluid-flow and mixed-volatile reactions with applications to regional metamorphism. *Contributions to Mineralogy and Petrology*, 106(3), 273–285. <https://doi.org/10.1007/BF00324557>

Acknowledgments

This study was supported by the National Key R&D Program of China (2018YFA0702701), National Science Foundation of China (Nos. 41490614, 41672059, and 41922013), and the State Key Laboratory of Lithospheric Evolution (SKL-Z202002). S.G. also acknowledges the supports from the Youth Innovation Promotion Association CAS (2017090). We thank Daniela Rubatto, Guanghai Shi, Francesca Piccoli, Ji'en Zhang, Meng Tian, Bo Wan, and Jingbo Liu for beneficial discussions. We also thank Thiha Soee and Jiangang Wang for the assistance during the field work, Guoqiang Tang and Xiaoxiao Ling for the SIMS analyses, Yijie Gao and Bin Su for the LA-ICP-MS analyses, Jiaqing Liu and Pan Tang for the CL analyses, and Di Zhang for the electron probe analyses. We gratefully acknowledge two anonymous reviewers and editor Stephen Parman for their detailed comments and suggestions that help significantly improve the manuscript.

- Baumgartner, L. P., Gerdes, M. L., Person, M. A., & Roselle, G. T. (1997). Porosity and permeability of carbonate rocks during contact metamorphism. In *Fluid Flow and Transport in Rocks* (pp. 83–98). Dordrecht: Springer
- Becker, J. A., Bickle, M. J., Galy, A., & Holland, T. J. (2008). Himalayan metamorphic CO₂ fluxes: Quantitative constraints from hydrothermal springs. *Earth and Planetary Science Letters*, *265*(3–4), 616–629. <https://doi.org/10.1016/j.epsl.2007.10.046>
- Bégué, F., Baumgartner, L. P., Bouvier, A., & Robyr, M. (2019). Reactive fluid infiltration along fractures: Textural observations coupled to in-situ isotopic analyses. *Earth and Planetary Science Letters*, *519*, 264–273. <https://doi.org/10.1016/j.epsl.2019.05.024>
- Bégué, F., Baumgartner, L. P., Müller, T., Putilz, B., & Vennemann, T. (2020). Metasomatic vein formation by stationary fluids in carbonate xenoliths at the eastern margin of the Bergell intrusion, Val Sissone, Italy. *Journal of Petrology*, *60*(12), 2387–2412. <https://doi.org/10.1093/petrology/egaa012>
- Bickle, M. J. (1996). Metamorphic decarbonation, silicate weathering and the long-term carbon cycle. *Terra Nova*, *8*(3), 270–276. <https://doi.org/10.1111/j.1365-3121.1996.tb00756.x>
- Bickle, M. J., & Baker, J. (1990). Advective-diffusive transport of isotopic fronts: An example from Naxos, Greece. *Earth and Planetary Science Letters*, *97*(1–2), 78–93. [https://doi.org/10.1016/0012-821X\(90\)90100-C](https://doi.org/10.1016/0012-821X(90)90100-C)
- Bucher-Nurminen, K. (1989). Reaction veins in marbles formed by a fracture-reaction-seal mechanism. *European Journal of Mineralogy*, *1*, 701–714. <https://doi.org/10.1127/ejm/1/5/0701>
- Caciagli, N. C., & Manning, C. E. (2003). The solubility of calcite in water at 6–16 kbar and 500–800 °C. *Contributions to Mineralogy and Petrology*, *146*(3), 275–285. <https://doi.org/10.1007/s00410-003-0501-y>
- Carter, L. B., & Dasgupta R. (2018). Decarbonation in the Ca-Mg-Fe carbonate system at mid-crustal pressure as a function of temperature and assimilation with arc magmas—Implications for long-term climate. *Chemical Geology*, *492*(5), 30–48. <https://doi.org/10.1016/j.chemgeo.2018.05.024>
- Cartwright, I. (1997). Permeability generation and resetting of tracers during metamorphic fluid flow: Implications for advection-dispersion models. *Contributions to Mineralogy and Petrology*, *129*(2–3), 198. <https://doi.org/10.1007/s004100050332>
- Chu, X., & Ague, J. J. (2013). Phase equilibria for graphitic metapelite including solution of CO₂ in melt and cordierite: Implications for dehydration, partial melting and graphite precipitation. *Journal of Metamorphic Geology*, *31*(8), 843–862. <https://doi.org/10.1111/jmg.12047>
- Chu, X., Lee, C. T. A., Dasgupta, R., & Cao, W. (2019). The contribution to exogenic CO₂ by contact metamorphism at continental arcs: A coupled model of fluid flux and metamorphic decarbonation. *American Journal of Science*, *319*, 631–657. <https://doi.org/10.2475/08.2019.01>
- Cliff, R. A., Yardley, B. W. D., & Bussy, F. (1993). U-Pb isotopic dating of fluid infiltration and metasomatism during Dalradian regional metamorphism in Connemara, western Ireland. *Journal of Metamorphic Geology*, *11*, 185–191. <https://doi.org/10.1111/j.1525-1314.1993.tb00141.x>
- Connolly, J. A. D. (1997). Devolatilization-generated fluid pressure and deformation-propagated fluid flow during prograde regional metamorphism. *Journal of Geophysical Research: Solid Earth*, *102*(B8), 18149–18173. <https://doi.org/10.1029/97JB00731>
- Cox, S. F. (2007). Structural and isotopic constraints on fluid flow regimes and fluid pathways during upper crustal deformation: An example from the Taemas area of the Lachlan Orogen, SE Australia. *Journal of Geophysical Research: Solid Earth*, *112*(B8), B08208. <https://doi.org/10.1029/2006JB004734>
- Evans, K. (2011). Metamorphic carbon fluxes: How much and how fast? *Geology*, *39*(1), 95–96. <https://doi.org/10.1130/focus012011.1>
- Ferry, J. M. (1994). A historical review of metamorphic fluid flow. *Journal of Geophysical Research: Atmospheres*, *99*(B8), 15487–15498. <https://doi.org/10.1029/94jb01147>
- Ferry, J. M. (2001). Calcite inclusions in forsterite. *American Mineralogist*, *86*(7–8), 773–779. <https://doi.org/10.2138/am-2001-0701>
- Ferry, J. M. (2016). Fluids in the crust during regional metamorphism: Forty years in the aterville limestone. *American Mineralogist*, *101*(3), 500–517. <https://doi.org/10.2138/am-2016-5118>
- Ferry, J. M., Winslow, N. W., & Penniston-Dorland, S. C. (2013). Re-evaluation of infiltration-driven regional metamorphism in northern New England: New transport models with solid solution and cross-layer equilibration of fluid composition. *Journal of Petrology*, *54*(12), 2455–2485. <https://doi.org/10.1093/petrology/egt053>
- Ganino, C., & Arndt, N. T. (2009). Climate changes caused by degassing of sediments during the emplacement of large igneous provinces. *Geology*, *37*(4), 323–326. <https://doi.org/10.1130/G25325A.1>
- Gao, S., Liu, X., Yuan, H., Hattendorf, B., Günther, D., Chen, L., et al. (2002). Determination of forty two major and trace elements in USGS and NIST SRM glasses by laser ablation-inductively coupled plasma-mass spectrometry. *Geostandards and Geoanalytical Research*, *26*(2), 181–196. <https://doi.org/10.1111/j.1751-908X.2002.tb00886.x>
- Gardiner, N. J., Searle, M. P., Morley, C. K., Robb, L. J., Whitehouse, M. J., Roberts, N. M. W., et al. (2018). The crustal architecture of Myanmar imaged through zircon U-Pb, Lu-Hf and O isotopes: Tectonic and metallogenic implications. *Gondwana Research*, *62*, 27–60. <https://doi.org/10.1016/j.gr.2018.02.008>
- Ghiorso, M. S., & Evans, B. W. (2008). Thermodynamics of rhombohedral oxide solid solutions and a revision of the Fe-Ti two-oxide geothermometer and oxygen-barometer. *American Journal of Science*, *308*(9), 957–1039. <https://doi.org/10.2475/09.2008.01>
- Green, E. C. R., Holland, T. J. B., & Powell, R. (2007). An order-disorder model for omphacitic pyroxenes in the system jadeite-diopside-hedenbergite-acmite, with applications to eclogite rocks. *American Mineralogist*, *92*(7), 1181–1189. <https://doi.org/10.2138/am.2007.2401>
- Groppo, C., Rolfo, F., Castelli, D., & Connolly, J. A. (2013). Metamorphic CO₂ production from calc-silicate rocks via garnet-forming reactions in the CFAS-H₂O-CO₂ system. *Contributions to Mineralogy and Petrology*, *166*(6), 1655–1675. <https://doi.org/10.1007/s00410-013-0947-5>
- Groppo, C., Rolfo, F., Castelli, D., & Mosca, P. (2017). Metamorphic CO₂ production in collisional orogens: Petrological constraints from phase diagram modeling of Himalayan, scapolite-bearing, calc-silicate rocks in the NKC(F)MAS(T)-HC system. *Journal of Petrology*, *58*(1), 53–83. <https://doi.org/10.1093/petrology/egx005>
- Guo, S., Chen, Y., Liu, C. Z., Wang, J. G., Su, B., Gao, Y. J., et al. (2016). Scheelite and coexisting F-rich zoned garnet, vesuvianite, fluorite in calc-silicate rocks from the Mogok metamorphic belt, Myanmar: Implications for metasomatism in marble and the role of halogens in W mobilization and mineralization. *Journal of Asian Earth Sciences*, *117*, 82–106. <https://doi.org/10.1016/j.jseaes.2015.12.004>
- Guo, S., Chen, Y., Ye, K., Su, B., Yang, Y. H., Zhang, L. M., et al. (2015). Formation of multiple high-pressure veins in ultrahigh-pressure eclogite (Hualiangting, Dabie terrane, China): Fluid source, element transfer, and closed-system metamorphic veining. *Chemical Geology*, *417*, 238–260. <https://doi.org/10.1016/j.chemgeo.2015.10.006>
- Guo, S., Ye, K., Chen, Y., & Liu, J. B. (2009). A normalization solution to mass transfer of multiple progressively altered samples using the Isocon diagram. *Economic Geology*, *104*(6), 881–886. <https://doi.org/10.2113/gsecongeo.104.6.881>

- Guo, S., Zhao, K. D., John, T., Tang, P., Chen, Y., & Su, B. (2019). Metasomatic flow of metacarbonate-derived fluids carrying isotopically heavy boron in continental subduction zones: Insights from tourmaline-bearing ultra-high pressure eclogites and veins (Dabie terrane, eastern China). *Geochimica et Cosmochimica Acta*, 253, 159–200. <https://doi.org/10.1016/j.gca.2019.03.013>
- Heaman, L. M., & LeCheminant, A. N. (1993). Paragenesis and U-Pb systematics of baddeleyite (ZrO₂). *Chemical Geology*, 110(1–3), 95–126. [https://doi.org/10.1016/0009-2541\(93\)90249-1](https://doi.org/10.1016/0009-2541(93)90249-1)
- Holland, T. J. B., & Powell, R. (1998). An internally consistent thermodynamic data set for phase of petrological interest. *Journal of Metamorphic Geology*, 16(3), 309–343. <https://doi.org/10.1111/j.1525-1314.1998.00140.x>
- Holland, T. J. B., & Powell, R. (2003). Activity–composition relations for phases in petrological calculations: An asymmetric multicomponent formulation. *Contributions to Mineralogy and Petrology*, 145, 492–501. <https://doi.org/10.1007/s00410-003-0464-z>
- Holness, M. B. (1997). Fluid flow paths and mechanisms of fluid infiltration in carbonates during contact metamorphism: The Beinn an Dubhaich aureole, Skye. *Journal of Metamorphic Geology*, 15(1), 59–70. <https://doi.org/10.1111/j.1525-1314.1997.00005.x>
- Jamtveit, B., Bucher-Nurminen, K., & Stijfhoorn, D. E. (1992). Contact metamorphism of layered shale-carbonate sequences in the Oslo Rift: I. Buffering, infiltration, and the mechanisms of mass transport. *Journal of Petrology*, 33(2), 377–422. <https://doi.org/10.1093/petrology/33.2.377>
- Jamtveit, B., Petley-Ragan, A., Incel, S., Dunkel, K. G., Aupart, C., Austrheim, H., et al. (2019). The effects of earthquakes and fluids on the metamorphism of the lower continental crust. *Journal of Geophysical Research: Solid Earth*, 124(8), 7725–7755. <https://doi.org/10.1029/2018JB016461>
- Jamtveit, B., Wogelius, R. A., & Fraser, D. G. (1993). Zonation patterns of skarn garnets: Records of hydrothermal system evolution. *Geology*, 21(2), 113–116. [https://doi.org/10.1130/0091-7613\(1993\)021<0113:ZPOSGR>2.3.CO.2](https://doi.org/10.1130/0091-7613(1993)021<0113:ZPOSGR>2.3.CO.2)
- Kerrick, D. M. (1977). The genesis of zoned skarns in the Sierra Nevada, California. *Journal of Petrology*, 18(1), 144–181. <https://doi.org/10.1093/petrology/18.1.144>
- Kerrick, D. M., & Caldeira, K. (1998). Metamorphic CO₂ degassing from orogenic belt. *Chemical Geology*, 145(3), 213–232. [https://doi.org/10.1016/S0009-2541\(97\)00144-7](https://doi.org/10.1016/S0009-2541(97)00144-7)
- Kessel, R., Schmidt, M. W., Ulmer, P., & Pettko, T. (2005). Trace element signature of subduction-zone fluids, melts and supercritical liquids at 120–180 km depth. *Nature*, 437(7059), 724–727. <https://doi.org/10.1038/nature03971>
- Li, Q. L., Li, X. H., Liu, Y., Tang, G. Q., Yang, J. H., & Zhu, W. G. (2010). Precise U-Pb and Pb-Pb dating of Phanerozoic baddeleyite by SIMS with oxygen flooding technique. *Journal of Analytical Atomic Spectrometry*, 25(7), 1107–1113. <https://doi.org/10.1039/B923444F>
- Li, X. H., Liu, Y., Li, Q. L., Guo, C. H., & Chamberlain, K. R. (2009). Precise determination of Phanerozoic zircon Pb/Pb age by multicollector SIMS without external standardization. *Geochemistry, Geophysics, Geosystems*, 10(4), Q04010. <https://doi.org/10.1029/2009GC002400>
- Li, X. H., Tang, G. Q., Gong, B., Yang, Y. H., Hou, K. J., Hu, Z. C., et al. (2013). Qinghu zircon: A working reference for microbeam analysis of U-Pb age and Hf and O isotopes. *Chinese Science Bulletin*, 58(36), 4647–4654. <https://doi.org/10.1007/s11434-013-5932-x>
- Liu, Y., Li, X. H., Li, Q. L., Tang, G. Q., & Yin, Q. Z. (2011). Precise U–Pb zircon dating at a scale of < 5 micron by the CAMECA 1280 SIMS using a Gaussian illumination probe. *Journal of Analytical Atomic Spectrometry*, 26, 845–851. <https://doi.org/10.1039/C0JA00113A>
- Ludwig, K. R. (2003). User's Manual for Isoplot 3.00: A Geochronological Toolkit for Microsoft Excel (Vol. 4, p. 74). Berkeley, CA: Berkeley Geochronology Center Special Publication.
- Manning, C. E. (1994). The solubility of quartz in H₂O in the lower crust and upper mantle. *Geochimica et Cosmochimica Acta*, 58(22), 4831–4839. [https://doi.org/10.1016/0016-7037\(94\)90214-3](https://doi.org/10.1016/0016-7037(94)90214-3)
- Manning, C. E., Shock, E. L., & Sverjensky, D. A. (2013). The chemistry of carbon in aqueous fluids at crustal and upper-mantle conditions: Experimental and theoretical constraints. *Reviews in Mineralogy and Geochemistry*, 75(1), 109–148. <https://doi.org/10.2138/rmg.2013.75.5>
- Menzies, C. D., Wright, S. L., Craw, D., James, R. H., Alt, J. C., Cox, S. C., et al. (2018). Carbon dioxide generation and drawdown during active orogenesis of siliciclastic rocks in the Southern Alps, New Zealand. *Earth and Planetary Science Letters*, 481, 305–315. <https://doi.org/10.1016/j.epsl.2017.10.010>
- Mitchell, A. H. G., Chung, S. L., Oo, T., Lin, T. H., & Hung, C. H. (2012). Zircon U-Pb ages in Myanmar: Magmatic-metamorphic events and the closure of a neo-Tethys ocean? *Journal of Asian Earth Sciences*, 56, 1–23. <https://doi.org/10.1016/j.jseas.2012.04.019>
- Mitchell, A. H. G., Htay, M. T., Htun, K. M., Win, M. N., Oo, T. H., & Hlaing, T. (2007). Rock relationships in the Mogok metamorphic belt, Tatkon to Mandalay, central Myanmar. *Journal of Asian Earth Sciences*, 29(5–6), 891–91. <https://doi.org/10.1016/j.jseas.2006.05.009>
- Penniston-Dorland, S. C., & Ferry, J. M. (2008). Element mobility and scale of mass transport in the formation of quartz veins during regional metamorphism of the Waits River Formation, eastcentral Vermont. *American Mineralogist*, 93(1), 7–21. <https://doi.org/10.2138/am.2008.2461>
- Putnis, A. (2009). Mineral replacement reactions. *Reviews in Mineralogy and Geochemistry*, 70, 87–124. <https://doi.org/10.2138/rmg.2009.70.3>
- Putnis, A., & Austrheim, H. (2010). Fluid-induced processes: Metasomatism and metamorphism. *Geofluids*, 10(1–2), 254–269. <https://doi.org/10.1111/j.1468-8123.2010.00285.x>
- Rolfo, F., Groppo, C., & Mosca, P. (2017). Metamorphic CO₂ production in calc-silicate rocks from the eastern Himalaya. *Italian Journal of Geosciences*, 136(1), 28–38. <https://doi.org/10.3301/IJG.2015.36>
- Rubatto, D., & Scambelluri, M. (2003). U-Pb dating of magmatic zircon and metamorphic baddeleyite in the Ligurian eclogites (Voltri Massif, Western Alps). *Contributions to Mineralogy and Petrology*, 146, 341–355. <https://doi.org/10.1007/s00410-003-0502-x>
- Searle, M. P., Garber, J. M., Hacker, B. R., Htun, K., Gardiner, N. J., Waters, D. J., et al. (2020). Timing of syenite-charnockite magmatism and ruby and sapphire metamorphism in the Mogok Valley Region, Myanmar. *Tectonics*, 39(3), e2019TC005998. <https://doi.org/10.1029/2019TC005998>
- Searle, M. P., Morley, C. K., Waters, D. J., Gardiner, N. J., Htun, U. K., Nu, T. T., et al. (2017). Tectonic and metamorphic evolution of the Mogok Metamorphic and Jade Mines belts and ophiolitic terranes of Burma (Myanmar). *Geological Society, London, Memoirs*, 48(1), 261–293. <https://doi.org/10.1144/M48.12>
- Searle, M. P., Noble, S. R., Cottle, J. M., Waters, D. J., Mitchell, A. H. G., Hlaing, T., et al. (2007). Tectonic evolution of the Mogok Metamorphic belt, Burma (Myanmar) constrained by U-Th-Pb dating of metamorphic and magmatic rocks. *Tectonics*, 26(3), TC3014. <https://doi.org/10.1029/2006TC002083>
- Skelton, A. (2011). Flux rates for water and carbon during greenschist facies metamorphism. *Geology*, 39(1), 43–46. <https://doi.org/10.1130/G31328.1>
- Skelton, A. (2013). Is orogenesis a net sink or source of atmospheric CO₂? *Geology Today*, 29(3), 102–107. <https://doi.org/10.1111/gto.12009>
- Sláma, J., Košler, J., Condon, D. J., Crowley, J. L., Gerdes, A., Hanchar, J. M., et al. (2008). Plešovice zircon—A new natural reference material for U–Pb and Hf isotopic microanalysis. *Chemical Geology*, 249(1–2), 1–35. <https://doi.org/10.1016/j.chemgeo.2007.11.005>

- Stewart, E. M., & Ague, J. J. (2018). Infiltration-driven metamorphism, New England, USA: Regional CO₂ fluxes and implications for Devonian climate and extinctions. *Earth and Planetary Science Letters*, 489, 123–134. <https://doi.org/10.1016/j.epsl.2018.02.028>
- Stewart, E. M., Ague, J. J., Ferry, J. M., Schiffries, C. M., Tao, R. B., Isson, T. T., et al. (2019). Carbonation and decarbonation reactions: Implications for planetary habitability. *American Mineralogist*, 104(10), 1369–1380. <https://doi.org/10.2138/am-2019-6884>
- Sun, S. S., & McDonough, W. F. (1989). Chemical and isotopic systematics of oceanic basalts: Implications for mantle composition and processes. *Geological Society, London, Special Publication*, 42(1), 313–345. <https://doi.org/10.1144/GSL.SP.1989.042.01.19>
- Svensen, H., & Jamtveit, B. (2010). Metamorphic fluids and global environmental changes. *Elements*, 6(3), 179–182. <https://doi.org/10.2113/gselements.6.3.179>
- Themelis, T. (2008). *Gems and Mines of Mogok* (pp. 0–352). Bangkok: A & T Publishers.
- Thu, Y. K., & Enami, M. (2018). Evolution of metamorphic fluid recorded in granulite facies metacarbonate rocks from the middle segment of the Mogok metamorphic belt in central Myanmar. *Journal of Metamorphic Geology*, 36(7), 905–931. <https://doi.org/10.1111/jmg.12419>
- Villa, I. M., & Williams, M. L. (2013). Geochronology of metasomatic events. In *Metasomatism and the Chemical Transformation of Rock*, Lecture Notes in Earth System Sciences (pp. 171–202). Berlin, Heidelberg: Springer. https://doi.org/10.1007/978-3-642-28394-9_6
- Whitney, D. L., & Evans, B. W. (2010). Abbreviations for names of rock-forming minerals. *American Mineralogist*, 95(1), 185–187. <https://doi.org/10.2138/am.2010.3371>
- Wiedenbeck, M., Alle, P., Corfu, F., Griffin, W. L., Meier, M., Oberli, F., et al. (1995). Three natural zircon standards for U-Th-Pb, Lu-Hf, trace element and REE analyses. *Geostandards Newsletter*, 19, 1–23. <https://doi.org/10.1111/j.1751-908X.1995.tb00147.x>
- Williams, I. S., Buick, I. S., & Cartwright, I. (1996). An extended episode of early Mesoproterozoic metamorphic fluid flow in the Reynolds Range, central Australia. *Journal of Metamorphic Geology*, 14(1), 29–47. <https://doi.org/10.1111/j.1525-1314.1996.00029.x>
- Win, M. M., Enami, M., & Kato, T. (2016). Metamorphic conditions and CHIME monazite ages of Late Eocene to Late Oligocene high-temperature Mogok metamorphic rocks in central Myanmar. *Journal of Asian Earth Sciences*, 117, 304–316. <https://doi.org/10.1016/j.jseas.2015.11.023>
- Wu, Y. B., Zheng, Y. F., Zhao, Z. F., Gong, B., Liu, X. M., & Wu, F. Y. (2006). U–Pb, Hf and O isotope evidence for two episodes of fluid-assisted zircon growth in marble-hosted eclogites from the Dabie orogen. *Geochimica et Cosmochimica Acta*, 70(14), 3743–3761. <https://doi.org/10.1016/j.gca.2006.05.011>
- Yardley, B. W. D., & Balashov, V. N. (1998). Modeling metamorphic fluid flow with reaction-compaction-permeability feedback. *American Journal of Science*, 298, 441–470. <https://doi.org/10.2475/ajs.298.6.441>
- Zhang, S., FitzGerald, J. D., & Cox, S. F. (2000). Reaction-enhanced permeability during decarbonation of calcite + quartz → wollastonite + carbon dioxide. *Geology*, 28(10), 911–914. [https://doi.org/10.1130/0091-7613\(2000\)28<911:RPDDOC>2.0.CO;2](https://doi.org/10.1130/0091-7613(2000)28<911:RPDDOC>2.0.CO;2)
- Zhang, S., Paterson, M. S., & Cox, S. F. (1994). Porosity and permeability evolution during hot isostatic pressing of calcite aggregates. *Journal of Geophysical Research*, 99(B8), 15741–15760. <https://doi.org/10.1029/94jb00646>
- Zhou, G., Wu, Y., Fu, B., Li, L., Zhang, W. X., & Zhang, Y. (2020). Genesis of baddeleyite and high δ¹⁸O zircon in impure marble from the Tongbai orogen, Central China: Insights from petrochronology and Hf-O isotope compositions. *Contributions to Mineralogy and Petrology*, 175(8), 1–20. <https://doi.org/10.1007/s00410-020-01714-z>